

AD 666245

32

MECHANISMS OF LASER-SURFACE INTERACTIONS

By

J. F. Ready

E. Bernal G.

L. T. Shepherd

SEMI-ANNUAL REPORT

To

Ballistic Research Laboratories

Aberdeen Proving Ground, Maryland

Contract No. DA-18-001-AMC-1040(X), Mod. 1

November 1967

This document has been approved
for public release and sale; its
distribution is unlimited.

DDC
RECEIVED
MAR 5 1968
C

Presented by

Honeywell Inc.

CORPORATE RESEARCH CENTER

Hopkins, Minnesota

Reproduced by the
CLEARINGHOUSE
for Federal Scientific & Technical
Information Springfield Va 22151

74

MECHANISMS OF LASER-SURFACE INTERACTIONS

By

J. F. Ready

E. Bernal G.

L. T. Shepherd

SEMI-ANNUAL REPORT

To

Ballistic Research Laboratories

Aberdeen Proving Ground, Maryland

Contract No. DA-18-001-AMC-1040(X) Modification No. 1

November 1967

"Delivered by Honeywell Inc., Research Center, pursuant to Contract No. DA-18-001-AMC-1040(X). Government's use controlled by the provisions of Articles 51 and 26 of Title II of the contract which are ASPR 9-107.2 and 9-203.1 and 9-203.4, respectively."

Presented by

Honeywell Inc.

CORPORATE RESEARCH CENTER

Hopkins, Minnesota

ABSTRACT

This report describes experimental and theoretical investigations of the particle emission produced in a laser-surface interaction. Measurements have been made on the angular distribution of ions emitted from a tungsten target irradiated by a ruby laser at flux densities around 10 to 20 megawatts/cm². In the plane perpendicular to the plane containing the incident laser radiation and normal to the target surface the number of ions emitted follows a $\cos^2 \theta$ distribution where θ is the angle from the normal to the target. In the plane containing the laser radiation and the target normal, most ions appear to be emitted within approximately 15° of the normal to the target. The energies of the ions are also maximum in the direction normal to the target and fall off as the angle from the normal increases. Calculations on a model for heating an alkali ion plasma by absorption of laser radiation indicate that runaway heating can occur at flux densities around 10⁹ watts/cm² with particle densities around 10¹⁸/cm³. The magnitudes and time histories of shock waves produced in nickel and carbon targets by absorption of laser radiation have also been calculated.

TABLE OF CONTENTS

<u>Section</u>		<u>Page</u>
I	Introduction	I-1
II	Experimental Work	II-1
	A. Noise in System	II-1
	B. Potentials in System	II-6
	C. Angular Distribution Measurements	II-12
	D. High Power Laser	II-24
III	Theoretical Work	III-1
	A. Comparison of Pulse Shapes with Free Expansion	III-1
	B. Plasma Heating	III-3
	C. Pressure Pulses	III-23
	D. Steady State Heating	III-29
IV.	Summary	IV-1

LIST OF ILLUSTRATIONS

<u>Figure</u>		<u>Page</u>
II-1	Noise in Signals in Interaction Chamber	II-2
II-2	Noise Occurring with Laser Double Pulse	II-3
II-3	Schematic Diagram for Noise Suppression	II-5
II-4	Effect of Potential on Target	II-7
II-5	Potential Distribution - Target above Ground	II-10
II-6	Potential Distribution - Target below Ground	II-11
II-7	Angular Distribution of Ions in Plane Perpendicular to Plane of Beam and Target Normal	II-14
II-8	Angular Distribution of Ions in Plane of Beam and Target Normal	II-15
II-9	Effect of Retarding Potential	II-17
II-10	Effect of Retarding Potential	II-18
II-11	Ion Arrival Times at Different Collectors	II-20
II-12	Ion Energy Distribution in Plane Perpendicular to Plane of Beam and Target Normal	II-21
II-13	Ion Energy Distribution in Plane of Beam and Target Normal	II-22
II-14	Ion Emission as Function of Laser Power	II-23
II-15	Scattering Centers in Damaged Ruby Rod	II-25
II-16	Twyman-Green Interferogram of Damaged Ruby Rod	II-26
III-1	Ion Pulse Shapes in Interaction Chamber	III-2
III-2	Calculated Plasma Temperature as a Function of Time	III-7
III-3	Calculated Sodium Ion Densities as Function of Time	III-10

<u>Figure</u>		<u>Page</u>
III-4	Calculated Sodium Ion Densities as Function of Time	III-12
III-5	Calculated Sodium Ion Densities as Function of Time	III-13
III-6	Pressure Pulses in Nickel	III-25
III-7	Pressure Pulses in Nickel	III-26
III-8	Pressure Pulses in Carbon	III-27
III-9	Pressure Pulses in Carbon	III-28
III-10	Temperature Profiles in Steady State Heating	III-33

SECTION I

INTRODUCTION

The investigations described in this report are continuations of work which have been carried out previously. These earlier investigations have been concerned with particle emission produced in laser-surface interactions. This work has been described in detail in previous reports. (1, 2, 3, 4, 5) Some knowledge of the background of this work, as discussed in the previous reports, is necessary for an understanding of the methods and aims of the investigations described in the present report. A time-of-flight spectrometer has been used to measure ion emission produced by absorption of ruby laser radiation with power densities of the order of 50 MW/cm^2 . The ions were found to be mainly alkali metals with energies of the order of several hundred electron volts. The neutral molecule emission produced under similar conditions has been studied with a quadrupole mass spectrometer and found to consist of thermally desorbed gases such as H_2 , CO , and CO_2 along with pulses of high energy neutral molecules having energies of the order of 100 eV.

In this report we describe our extension of these measurements. The bulk of the experimental work reported here has been carried out in an interaction chamber with collectors around the periphery of the hemisphere which has the laser-illuminated target at its center. Measurements of the angular distribution indicate that there is a maximum in both the number of ions and the ion energy in a direction normal to the target surface, and that both these quantities fall off as the angle from the normal increases. Moreover, if one looks in the plane defined by the direction of the laser beam and the normal to the target surface, one obtains a different angular distribution than for the plane perpendicular to this.

As we shall see later, there have been considerable problems with noise in obtaining this data. The essential criterion for obtaining good data on this system appears to be the use of relatively low laser flux densities. This means that this system may not be so useful for obtaining data at high laser flux densities as we had at one time hoped.

On the theoretical side we have carried out an analysis of the model in which the plasma was heated by absorption of laser radiation in a plasma of alkali ions with little coupling of energy to the desorbed neutral gases. This picture contained many physically appealing features and was in accord with our experimental data. However, the computer analysis indicates that heating takes place only at laser flux densities and at alkali ion densities which are uncomfortably high. Therefore, the results of this analysis are essentially negative and it appears that invoking this mechanism is not sufficient to explain heating of the blowoff material at laser flux densities below 100 megawatts/cm².

We have also extended calculation of the pressure pulses produced by thermomechanical shock waves induced in the target material by absorption of the laser radiation. Using the PUFF computer code we have calculated the time history of the stress profiles for nickel and carbon targets.

Finally, we have calculated steady-state heating for thin metallic targets. This topic has become of interest with the advent of high power carbon dioxide lasers. The results indicate that for a proper choice of target material, the CO₂ laser can be a valuable tool in studying the laser-surface interaction.

SECTION II

EXPERIMENTAL WORK

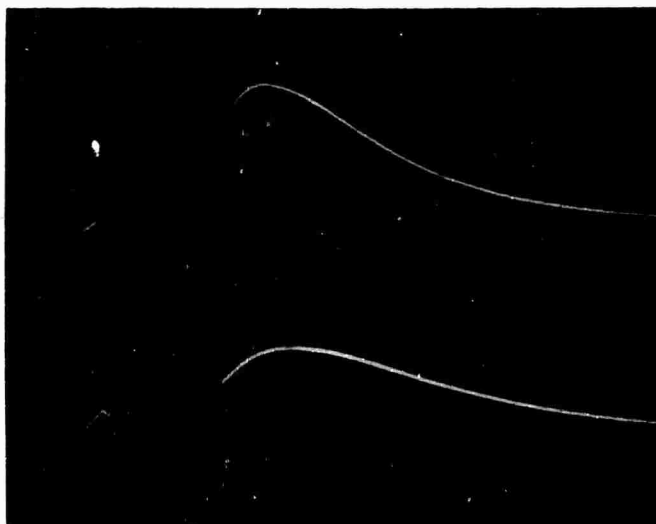
The bulk of the experimental work in this report period has been performed in the hemispherical interaction chamber which has collectors arranged around the periphery of the hemisphere and a target at the center. The only target material used to date has been tungsten. A considerable amount of data has been collected using this system. Measurements have been obtained for the angular distribution of the ions emitted from the tungsten target irradiated by high power pulses of Q-switched ruby laser radiation.

A. NOISE IN SYSTEM

There have been a considerable number of problems in the operation of the system. The main problem has been that of noise. The data obtained from the collectors has frequently been noisy. A typical example is shown in Figure II-1. It shows two photographs of high frequency oscillations near the beginning of pulses from the output of the collector located along the normal to the target surface and from the hemisphere. These oscillations often mask the form of the output signal and blot out portions of it. The persistent presence of the high frequency oscillations has been very troublesome in obtaining good data using this system.

The noise problem is particularly apparent when the laser double pulses. This is shown in Figure II-2 which shows two photographs of the output when the laser emitted a second pulse. In the upper photograph the second pulse occurred about 30 microseconds after the first pulse, and in the lower photograph about 20 microseconds later. The emission from the first pulse is relatively noise free; then at the beginning of the emission produced by the second laser pulse there are high frequency oscillations

A



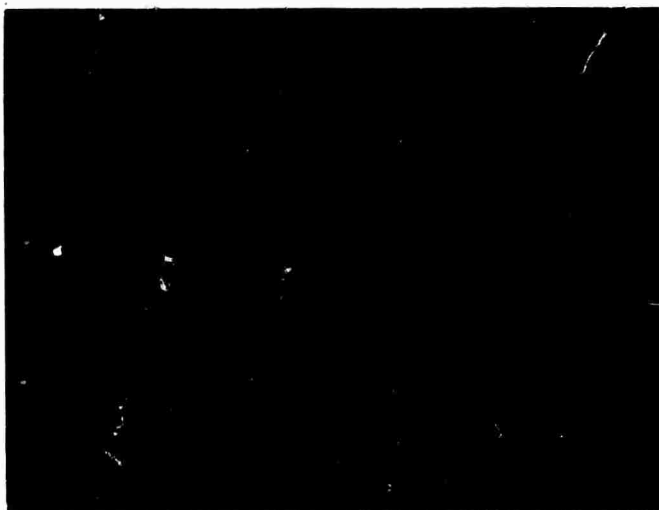
B



Figure II-1 - Noise in Signals from Interaction Chamber

- A. $2\mu\text{s}/\text{cm}$. Top trace $0.02\text{V}/\text{cm}$ from collector along normal to target. Bottom trace $10\text{V}/\text{cm}$ from hemisphere.
- B. $0.02\text{V}/\text{cm}$, $5\mu\text{s}/\text{cm}$. Top trace from collector at 15° from normal to target. Bottom trace from collector along normal to target.

A



B

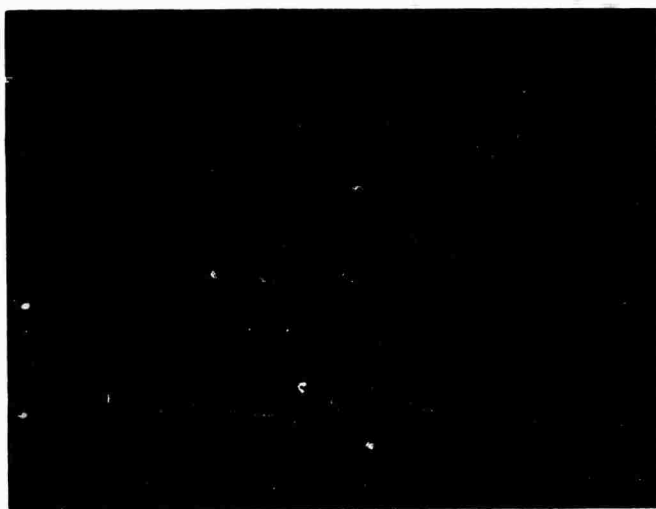


Figure II-2 - Noise in Signals from Interaction Chamber Due to Laser Double Pulse

- A. $5\mu\text{s}/\text{cm}$. Top trace $0.005\text{V}/\text{cm}$ from collector at 45° from normal to target. Bottom trace $0.02\text{V}/\text{cm}$ from collector along normal to target.
- B. $5\mu\text{s}/\text{cm}$. Top trace $0.005\text{V}/\text{cm}$ from collector at 15° from normal to target. Bottom trace $0.02\text{V}/\text{cm}$ from collector along normal to target.

Since the second laser pulse was smaller than the first and produced less particle emission, it is possible that the noise originates in interaction of the radiation with the blowoff material so that the system is particularly prone to noise when there has been particle emission produced a short time before a laser pulse comes in.

We have tried a number of techniques for noise suppression. One of these is shown in Figure II-3 which shows a schematic diagram of the hemispherical interaction chamber with the target and the collector. Ions traveling from the target to the hemisphere pass through the grid to the collector giving rise to a voltage signal at point A on the oscilloscope preamplifier. If noise results from a common mode or ground loop or in pickup in the oscilloscope leads, it could be eliminated by a differential measuring technique. We put the inputs A and -B from the oscilloscope preamp at point 1 and adjust the gain of A and -B for zero output from the sum of A and -B using short leads coiled around each other. We then move -B to point 2 and take the measurements. We find that this technique makes no difference in the output results and conclude that the noise is not a spurious effect caused by pickup in the electronic circuitry. It may originate in oscillations induced by movement of charge in the target-collector-hemisphere system. At present we do not understand well the origin of this noise.

The noise can be eliminated by operation of the laser at a relatively low power so that the laser flux density at the position of the target is less than approximately 20 megawatts/cm². At this level we obtain clean output pulses from the collector such as are shown in early portions of the oscilloscope traces in Figure II-2. Whenever the laser flux density is kept below this level good data is obtained from the collectors except in the case where the laser double pulses and the emission produced by the second pulse is noisy. However, even when the laser double pulses data can be obtained from the early portion output of the collector since the interesting phenomena occur before the second laser pulse.

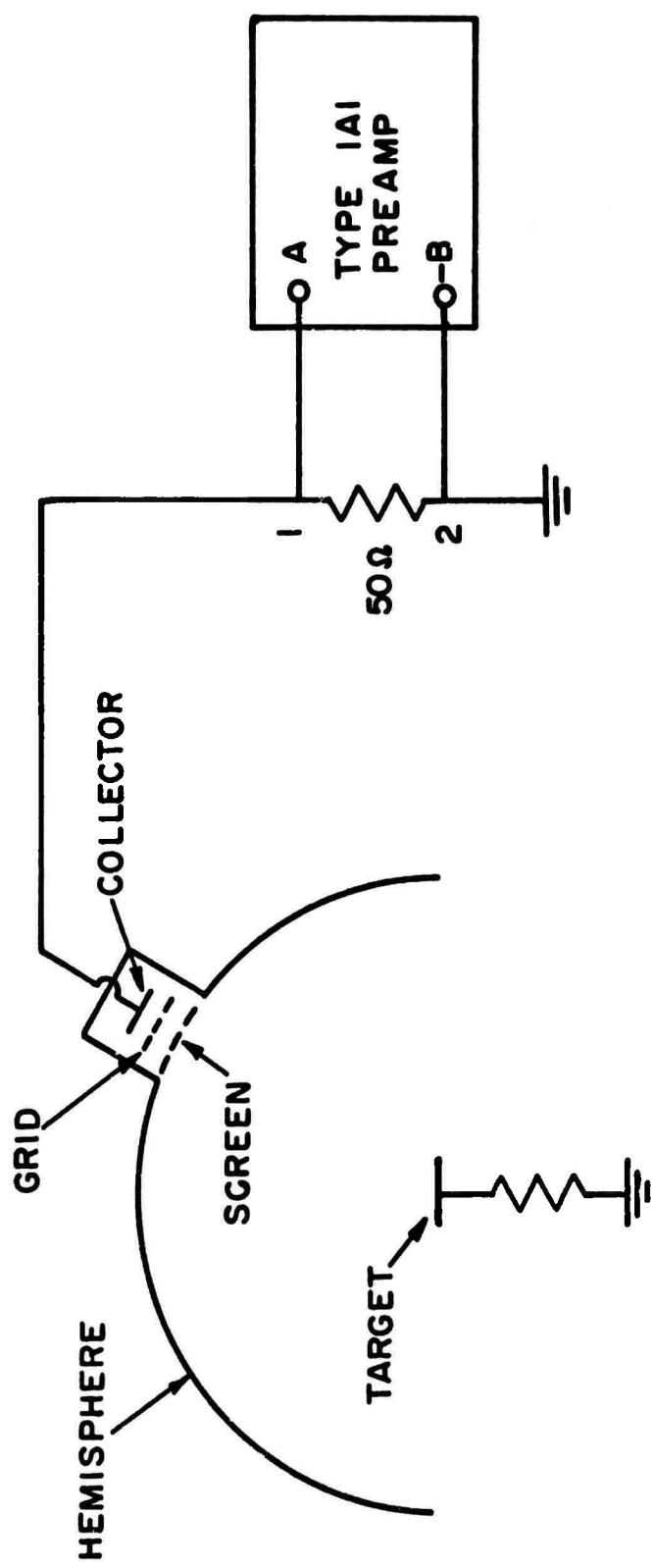


Figure II-3 - Schematic Diagram for Noise Suppression

Since the oscillations are of much higher frequency than the frequencies of the desired signals, filtering techniques may improve the situation.

This limitation on operating flux density means that the usefulness of the interaction chamber may be limited and that we could use it for only certain ranges of laser power. Above that power, high frequency high amplitude oscillations which block out a portion of the signal make the obtaining of good data difficult. Thus, we may not be able to use this interaction chamber to extend the operating range of laser powers in this study as we had hoped to do.

B. POTENTIALS IN SYSTEM

The effect of applying a potential to the target was investigated. We held the target at a positive potential with respect to the hemisphere, i. e., an ion accelerating field. Some typical results are shown in Figure II-4. The top photograph was taken at 0 accelerating potential, the middle photograph of 270 volts; and the bottom photograph at 540 volts. In each of these photographs the upper trace is from the collector along the normal to the target, and the bottom trace is from the hemisphere. Both were taken across 50 ohm resistors and fed into the oscilloscope. The sweep speeds of all these photographs are five microseconds per cm. On the top photograph the vertical sensitivity of the top trace is 0.1 volts/cm, the lower trace .1 volt/cm. In the middle and bottom photographs the top traces are 0.1 volts/cm, and the bottom traces are 10 volts/cm. The top photograph shows the behavior that one expects from the system.⁽⁵⁾ In the lower trace one sees displacement current at the hemisphere beginning essentially at the time of the laser pulse and rising to a peak at the time the charge begins to arrive at the position of the hemisphere as shown by the break in the trace from the collector. The relative shapes of these two traces are easy to understand. However, the relative amplitudes are somewhat puzzling in that the solid angle subtended by the collector is much smaller ($\sim 10^{-3}$)

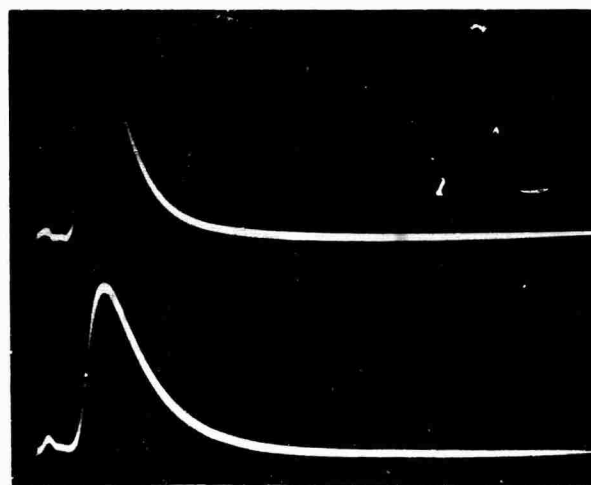
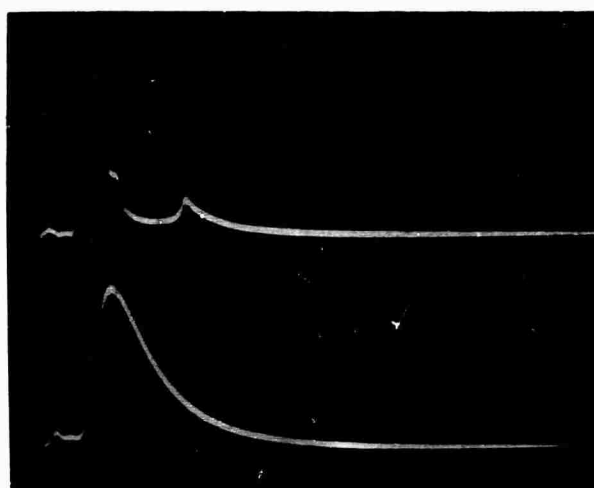
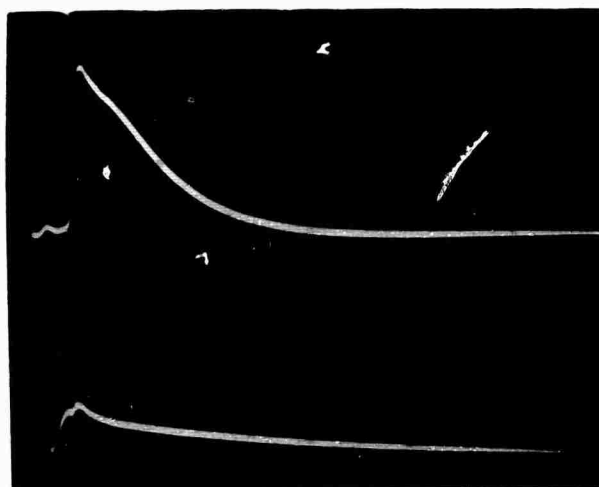


Figure II-4 - Effect of Potential Applied to Target. Sweep speed: $5\mu\text{s}/\text{cm}$. Upper traces from collector along normal to target. Bottom traces from hemisphere. All upper traces are $0.1\text{V}/\text{cm}$. In the top photograph the bottom trace is $0.1\text{V}/\text{cm}$; in the middle and bottom photographs the lower traces are $10\text{V}/\text{cm}$.

than the solid angle subtended by the hemisphere, but the amplitudes of the signals are different by only a factor of 3. Part of this is no doubt due to the emission being peaked in the direction normal to the surface; however, this effect cannot explain all of the relative differences.

When 270 volts are applied to the target, some rather surprising results are obtained. The results, as shown in the middle photograph, are reproducible and can be obtained when one goes back to the same condition day after day. The signal arriving at the hemisphere increased by two orders of magnitude and the shape is changed. The little bump at the beginning may possibly be a remnant of the original shape as shown in the top photograph. However the main current arriving at the hemisphere appears to be delayed by approximately the drift time of the plasma to the hemisphere. It has a shape very similar to that shown for the pulse shape at the collector in the top photograph. Moreover, the pulse shape at the collector has become rather odd. It shows a rapid decrease after it reaches the peak. Some irregular bumps follow the peak.

When the voltage is raised to 540 volts, the pulse shape at the collector again becomes regular and has approximately the same shape as when no voltage is applied to the target. Increasing the target voltage to 540 volts does not appreciably change the shape of the pulse at the hemisphere as compared to its shape at 270 volts. This also is rather surprising since one would expect the charge to pass across the gap more quickly as the accelerating voltage is raised.

One might be able to explain the behavior of the pulse shape at the hemisphere by assuming a plasma that drifts most of the way across the gap between target and hemisphere without charge separation. At higher voltages it is pulled apart after it has expanded to a certain point so that the displacement current effects do not show up in the bottom two photographs of Figure II-4. This also would explain the large increase in the pulse size at the hemisphere

as one applies an accelerating voltage for ions, and it would explain the small dependence of the time of the arrival of this pulse on the accelerating voltage. However, if this were the case, one would expect the pulse size at the collector to be increased considerably also, whereas the collector pulse size is almost independent of the voltage applied to the target. Moreover, there is no satisfactory explanation regarding the anomalous behavior of the collector trace at 270 volts. At this stage there are a range of phenomena in the interaction chamber which we cannot adequately interpret.

We investigated the field profiles in the chamber as voltage was applied to the target. Equipotential surfaces in the angular distribution chamber were determined using an analog method. The electrode configuration of the chamber was drawn on a sheet of conducting paper using silver paste, and appropriate voltages were applied to the different electrodes. One of the two terminals of a high impedance probe, such as an oscilloscope, was tied to a point while the other one was moved in the region between the electrodes. The equipotential lines are then obtained by following the lines along which nulls in the potential difference between the two probes are located. Such equipotential surfaces are of use in interpreting the angular distribution measurements that are made with a potential difference between the target and other electrodes in the chamber.

The equipotential surfaces were determined for two different potential configurations. The first configuration is shown in Figure II-5. In this case the target is held at a positive potential of +10 volts, while the hemisphere and outer shell of the chamber are held at ground potential. It is obvious from the figure that, except in the immediate neighborhood of the target, the electric field is radial at all points of interest in the chamber. The second configuration is one in which the target and outer shell of the chamber are held at ground potential while the hemisphere is held at a potential of -10 volts. The resulting equipotential surfaces are shown in Figure II-6. In this case it is obvious that there are large tangential components of electric field even at points far removed from the target.

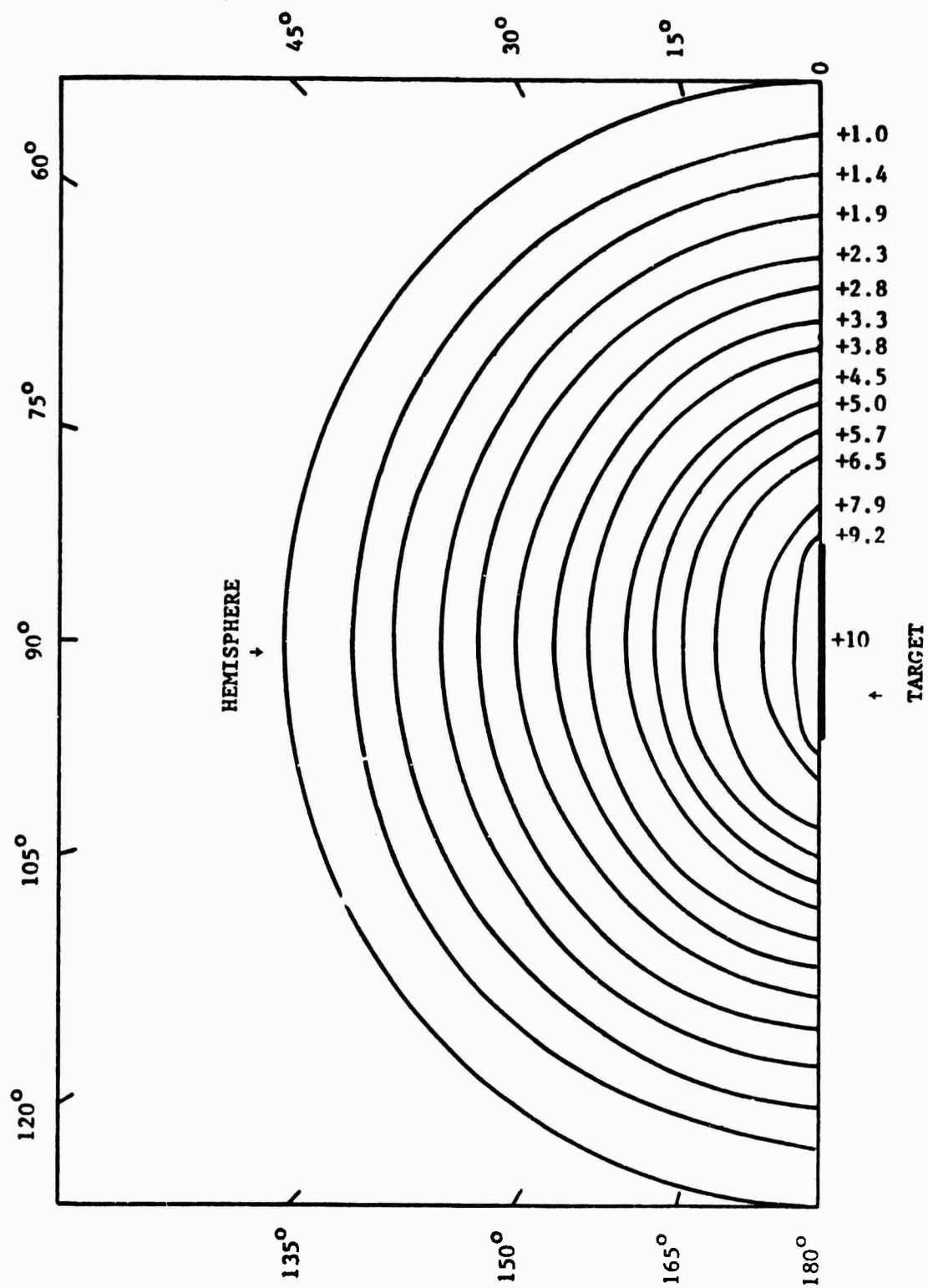


Figure II-5 - Potential Distribution in Interaction Chamber With Target at +10 Volts and all Other Electrodes at Ground.

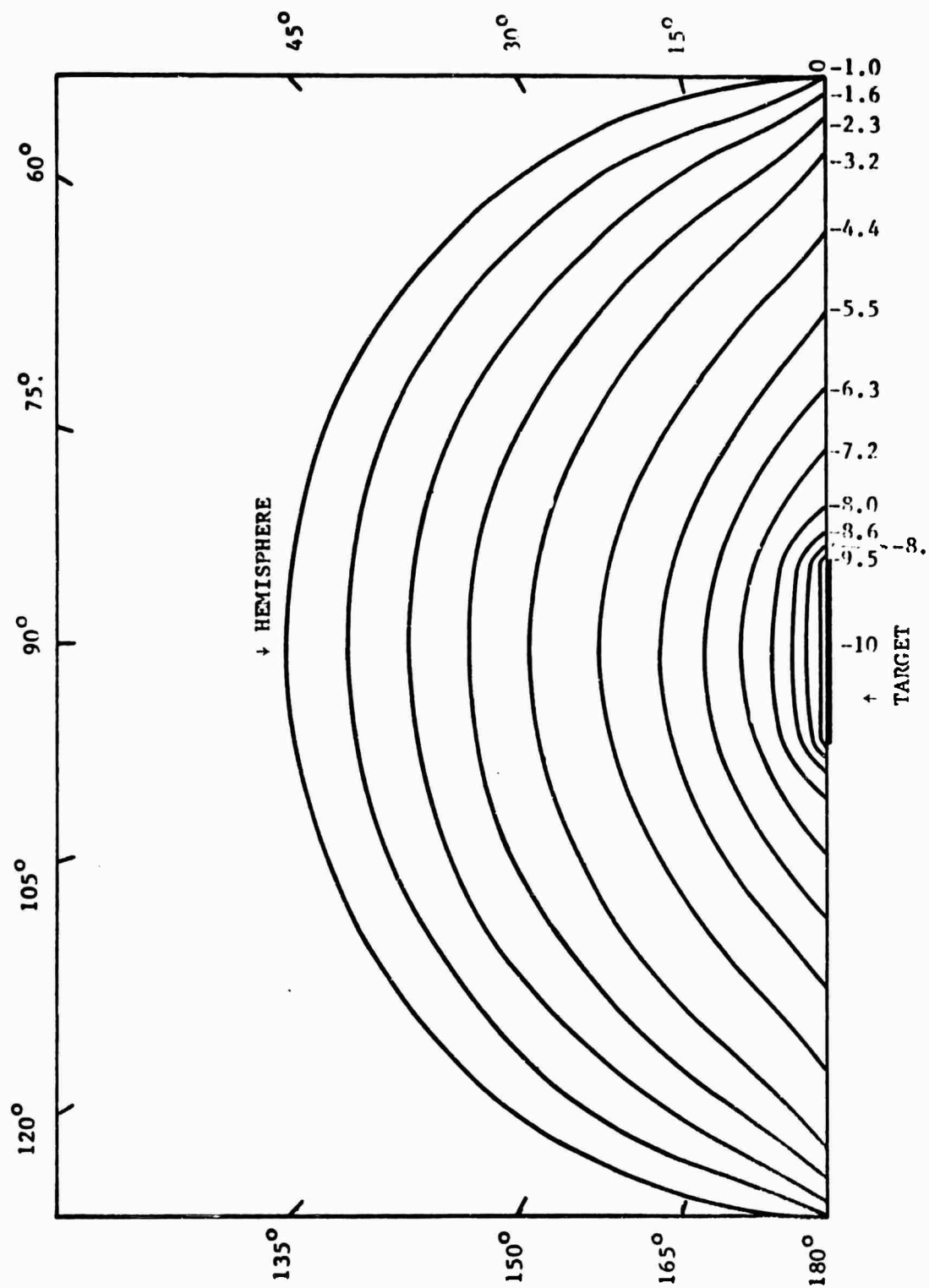


Figure II-6 - Potential Distribution in Interaction Chamber With Target at -10 Volts and all Other Electrodes at Ground.

The above results indicate that if potential differences are to be applied between the target and the hemisphere, the following precautions should be observed in order to minimize the distortion of the angular distribution of particles that will be detected at the hemisphere: (a) the hemisphere and the outer shell of the chamber should be held at the same potential if at all possible, (b) a fairly good approximation to a radial field can be obtained by minimizing the size of the target.

Since with an applied voltage the field lines that run out from the target to the hemisphere are somewhat distorted, it is only at zero applied potential to the target that a really symmetric case is obtained. This indicates that the best data on the system should be that obtained at zero accelerating potential. It is difficult to see how the results obtained in Figure II-4 can result from a distortion of the field lines such as are shown in Figure II-5 and Figure II-6. However, it does indicate that possibly the best results are those in the top photograph of Figure II-4. The angular distributions were accordingly measured with no potential applied to the target.

C. ANGULAR DISTRIBUTION MEASUREMENTS

Working at low laser powers so that the data were free of noise, we have measured the angular distribution of ions emitted from the target in the interaction chamber. Using the different collectors on the circumference of the hemisphere and taking the ratio of the signal from a detector at a particular angle to the signal from the detector along the normal to the target surface gives the angular distribution normalized to the value perpendicular to the surface as unity. From shot to shot at constant laser power the signal received at the detector in the direction normal to the surface is approximately constant. Preliminary results ⁽⁵⁾ indicated an anisotropic distribution with more material emitted at 75° than at 90° to the surface. More complete data has not confirmed this preliminary result. The maximum amount of emission is in the direction normal to the surface and the amount falls off as the angle from the direction to the normal increases.

We have obtained the angular distribution in two planes perpendicular to each other and both perpendicular to the target surface. Since the laser beam strikes

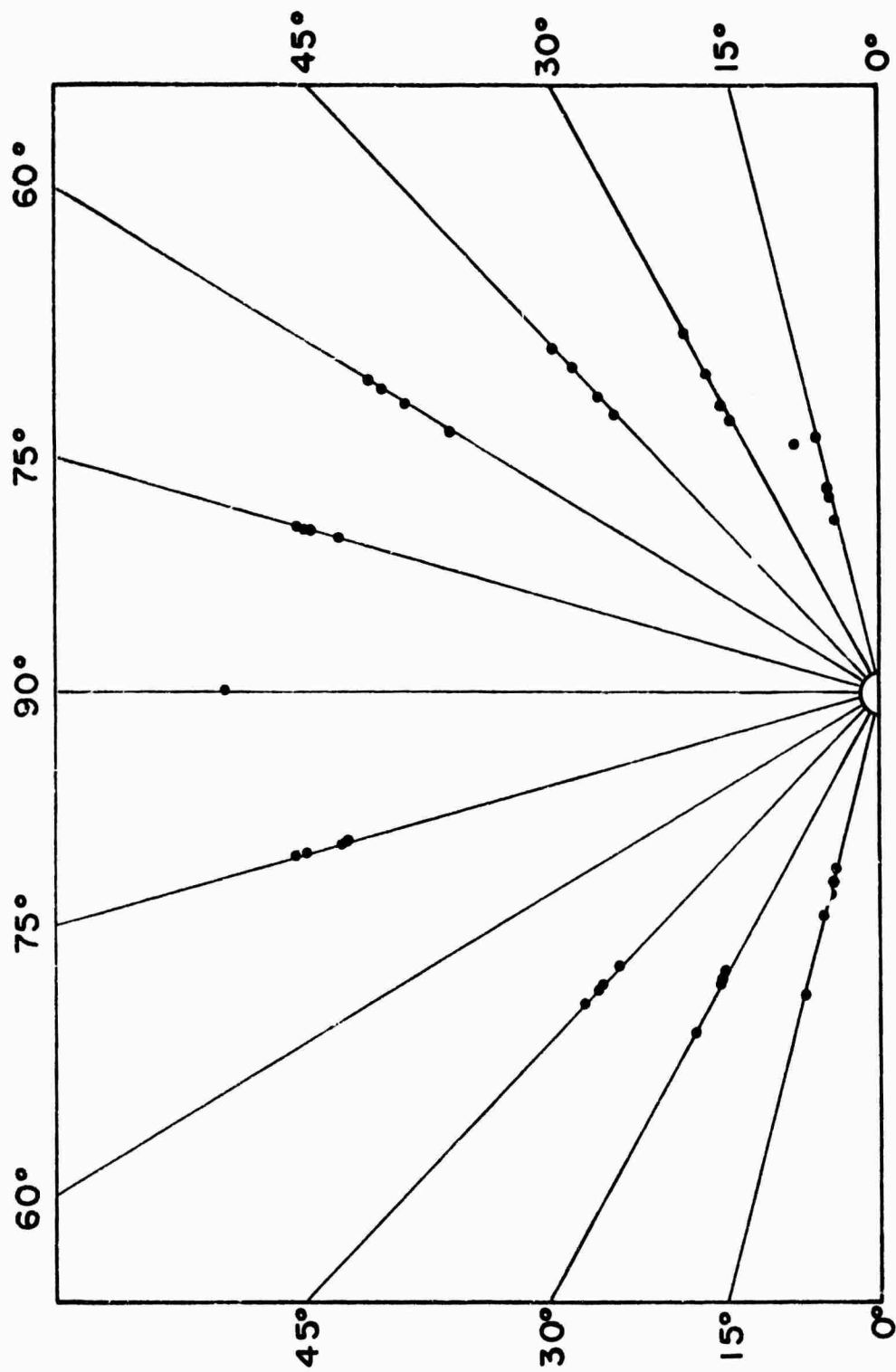
the target at an oblique angle, the direction of the beam and the normal to the target define a plane, which is one of the planes in which we made measurements. The other plane is perpendicular to the first and also contains the normal to the target surface. In what follows we shall refer to these two planes respectively as the plane containing the beam and target normal and the plane perpendicular to the plane containing the beam and target normal

The results are shown in Figures II-7 and II-8. The data are the integrated emission (i. e. area under the curve) for a particular direction divided by the ion emission from the collector along the normal to the target. The normalization reduces scatter due to shot to shot variations in laser power.

Figure II-7 shows the angular distribution of ions in the plane perpendicular to the plane containing the beam and the target normal. The angular distribution follows approximately a $\cos^2 \theta$ distribution where θ is the angle between the direction of observation and the normal to the surface, and is symmetric about $\theta = 0$. There is some scatter in this data from shot to shot, but the general trend of the data is well apparent.

Figure II-8 shows data for the plane containing the laser beam and the target normal. The amount of scatter has increased considerably and the angular distribution has become more complicated. We regard the data for this plane as still being preliminary and subject to future confirmation. The results in Figure II-8 indicate an asymmetry about the normal to the target surface. The laser beam enters at an angle equal to 30° from the target normal through the hole which would ordinarily house a collector in that direction so that no data were obtained at that angle. At 30° from the target normal on the opposite side of the normal in the same plane, the laser light reflected from the target struck the collector. No good data were obtainable from this collector; this collector gave an output much more noisy than the other collectors. Apparently the reflected laser light was causing particle emission from this collector. Accordingly, no data are given for this angle in Figure II-8.

From Figure II-8 it appears as if the emission with a component along the forward direction in which the laser beam is traveling is somewhat less than in the backward direction, at least at the angle 15° from the normal of the target surface. At angles 45° and greater from the normal to the target in both the



ANGULAR DISTRIBUTION

Figure II-7 - Angular Distribution of Ion Emission in Plane Perpendicular to Plane Containing Laser Beam and Target Normal.

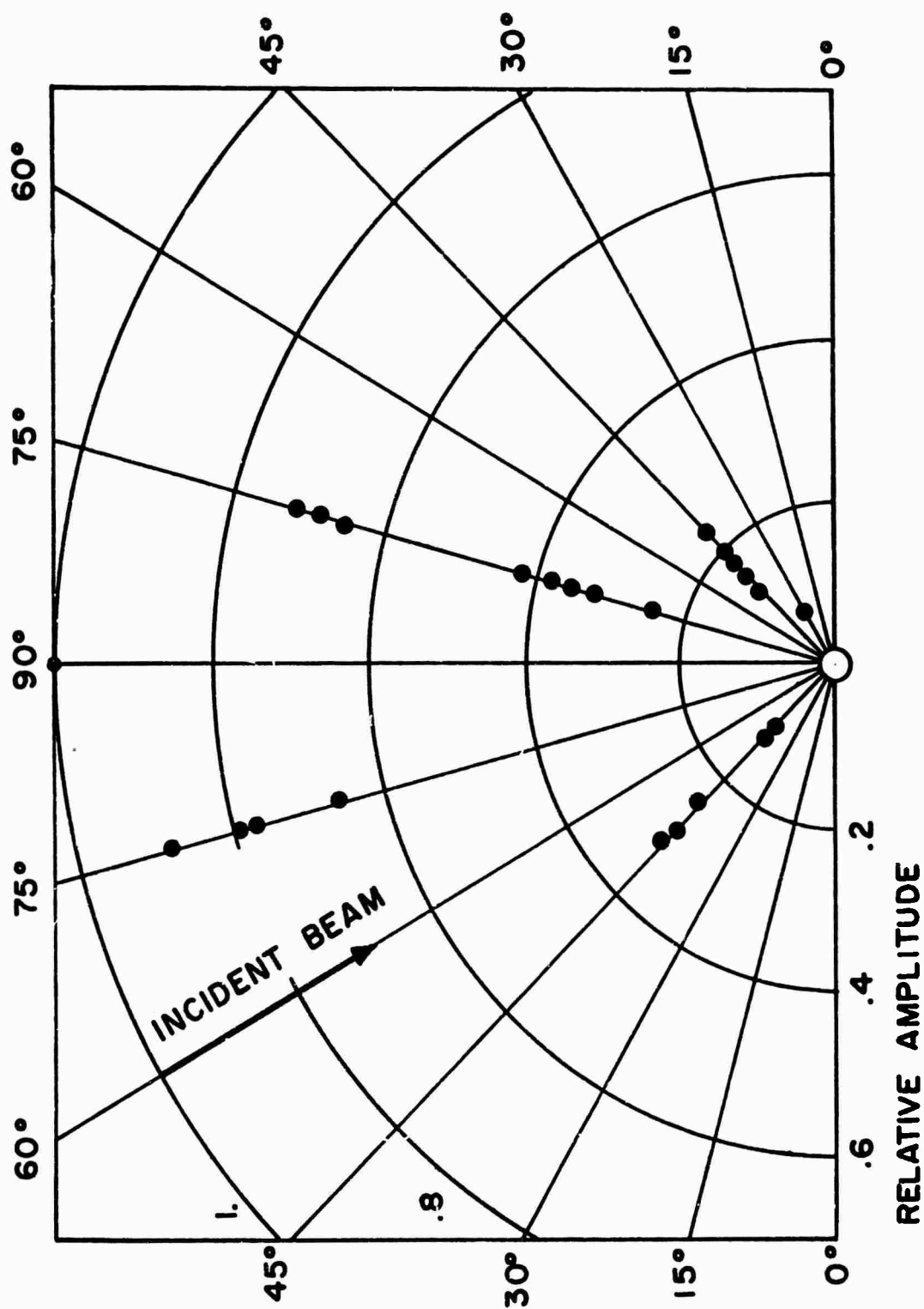


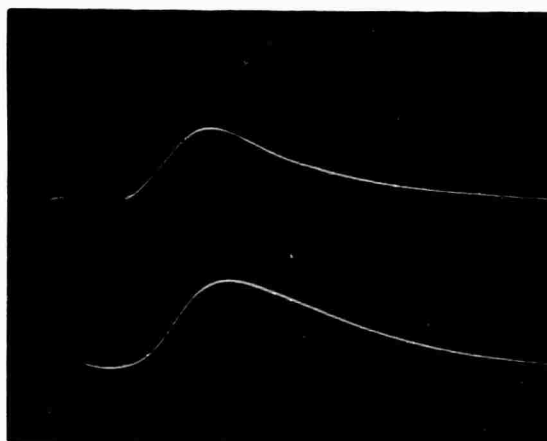
Figure II-8 - Angular Distribution of Ion Emission in Plane Containing Laser Beam and Target Normal.

forward and back directions the emission dropped off to smaller values, so small in fact at 60° and 75° that it was virtually unmeasurable and only one point is shown in Figure 11-8 for these angles. It appears as if the emission in the plane is concentrated in an angular spread approximately 15° from the normal to the surface and very little emerges at larger angles. It is unfortunate that the data at 30° to the target normal is not obtainable since this would fall in the intermediate region between relatively large and relatively small values.

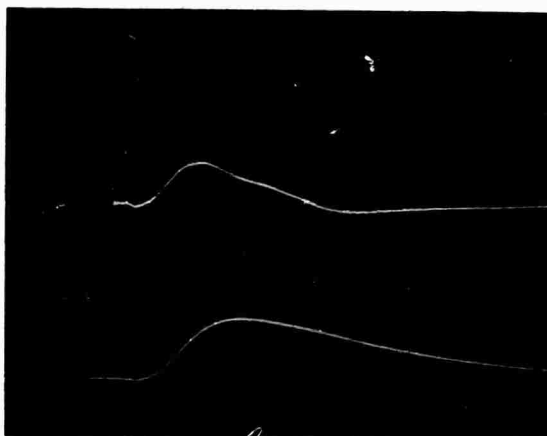
The data shown in Figures 11-7 and 11-8 were both taken with the polarization of the laser beam in the plane containing the incident laser beam and the target normal. In the future we shall take data with the laser polarization perpendicular to this plane. It is not immediately apparent that this change should cause a difference in the emission but it is a point worth checking.

Retarding potential measurements have also been carried out. Results indicate that the signal at the collectors can be eliminated by application of a voltage in the range of 270 to 360 volts. This voltage is applied on the retarding electrode which lies between the screen in the hemisphere hole and the collecting electrode. The screen across the hemisphere hole shields ions traveling between the target and the hemisphere from the effect of this potential so that it is felt only by ions that have penetrated through the screen. Figures 11-9 and 11-10 show some oscilloscope traces with a series of increasing applied retarding potentials. The results are essentially in agreement with the results of measurements from the time of flight spectrometer for the energy of ions produced under similar circumstances. However, we note that even at high applied voltages on the retarding grids there remains some residual signal at the collector. We have not been able to explain this signal. It appears to be independent of conditions in the chamber. At 270 volts retarding potential the smooth shape of the collector has become bumpy and the tail of the pulse has apparently been cut off.

A



B

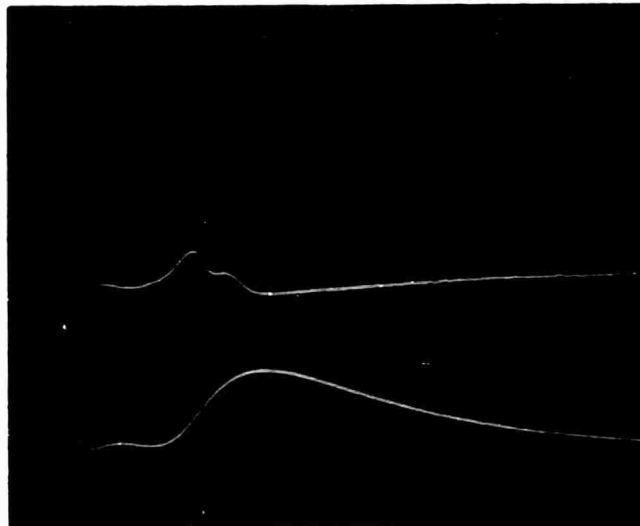


C



Figure II-9 - Effect of Retarding Potential. Sweep speed: $2\mu\text{s}/\text{cm}$. Top Traces From Collector Along Normal to Target, $0.02\text{V}/\text{cm}$. Bottom Traces From Hemisphere, $10\text{V}/\text{cm}$.
A. 0 volts retarding potential.
B. 90 volts retarding potential.
C. 180 volts retarding potential.

D



E

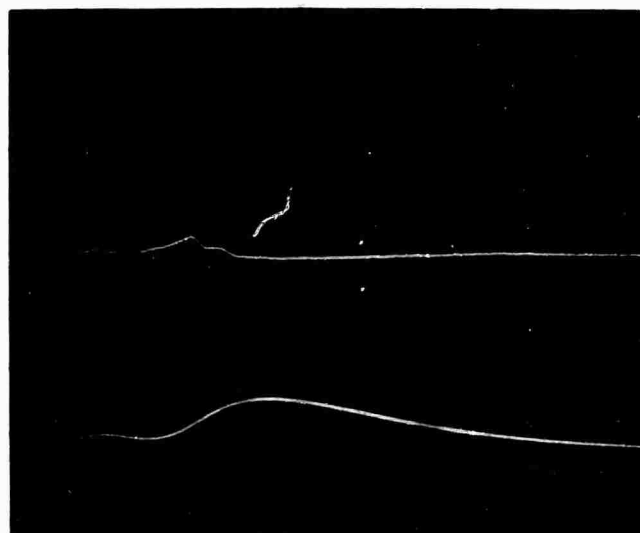


Figure II-10 - Effect of Retarding Potential. Sweep speed: $2\mu\text{s}/\text{cm}$. Top Traces From Collector Along Normal to Target, $0.02\text{V}/\text{cm}$. Bottom Traces From Hemisphere, $10\text{V}/\text{cm}$.
D. 270 volts retarding potential.
E. 360 volts retarding potential.

The angular distribution of ion energies has not yet been investigated by the retarding potential technique. We shall undertake this in the future. However, some information is available from the same data that were obtained in measurements of the angular distribution of particles. A typical oscilloscope trace of the output from two different collectors is shown in Figure II-11. In A the upper trace is the emission from a collector at an angle of 15° from the normal to the target, and in B the upper trace is from a collector at an angle of 75° from the normal and in the plane containing the beam and the normal. Both lower traces are from the collector along the normal to the target. Both the amplitudes and arrival times change as we move farther away from the normal. The arrival times at the collectors at large oblique angles are later, that is, they correspond to lower ion energies. In Figure II-12 we plot the relative energy, as derived from the square of the ratios of the arrival times (i. e., the time at which the peaks of the pulses occur) as a function of angle from the normal for the plane perpendicular to the plane containing the beam and the normal. In Figure II-13 we show the same results for the plane containing the beam and the target normal. These preliminary results show that there is a variation in energy of the ions as a function of angle of emission.

The results in Figure II-12 are relatively isotropic, but in Figure II-13 the energies appear to be maximum in a cone of 15° around the normal to the target. There is scatter which is caused by variations in the pulse shapes from one shot to another.

We have also investigated the relative numbers of particles emitted as a function of laser power. Figure II-14 shows the integrated ion current from the collector normal to the target surface as a function of laser power in relative units. There is a considerable amount of scatter in this data but unmistakably the general trend is monotonically increasing. There is a threshold below which no emission is detectable.

A



B

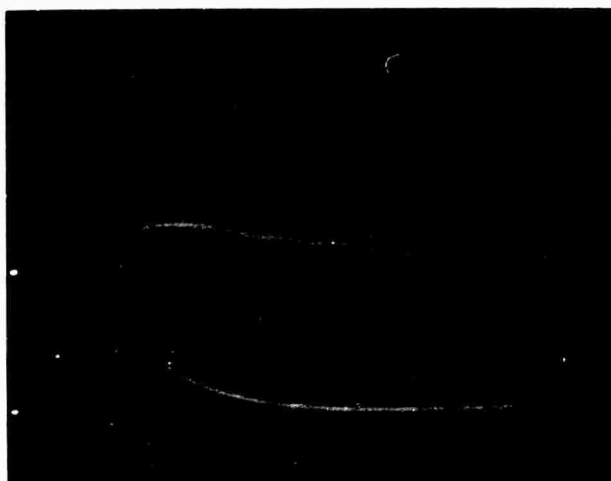


Figure II-11 - Ion Arrival Times. Sweep speeds: $5\mu\text{s}/\text{cm}$.

- A. Upper Trace: $0.01\text{V}/\text{cm}$ from collector at 15° from normal to target in plane containing laser beam and normal to target.
Lower trace: $0.01\text{V}/\text{cm}$ from collector along normal to target.
- B. Upper trace: $0.005\text{V}/\text{cm}$ from collector at 45° from normal to target in plane containing laser beam and normal to target.
Lower trace: $0.02\text{V}/\text{cm}$ from collector along normal to target.

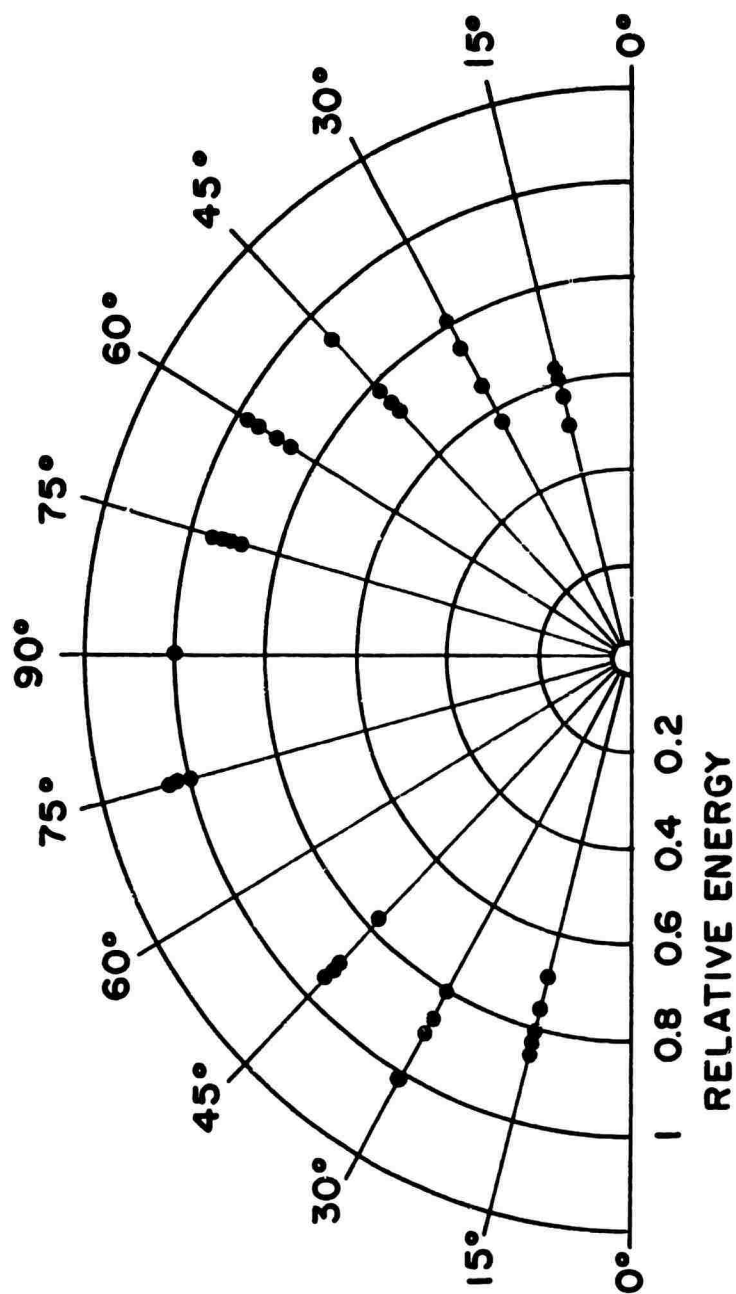


Figure II-12 - Ion Energy Distribution In Plane Perpendicular To Plane Containing Laser Beam and Normal To Target

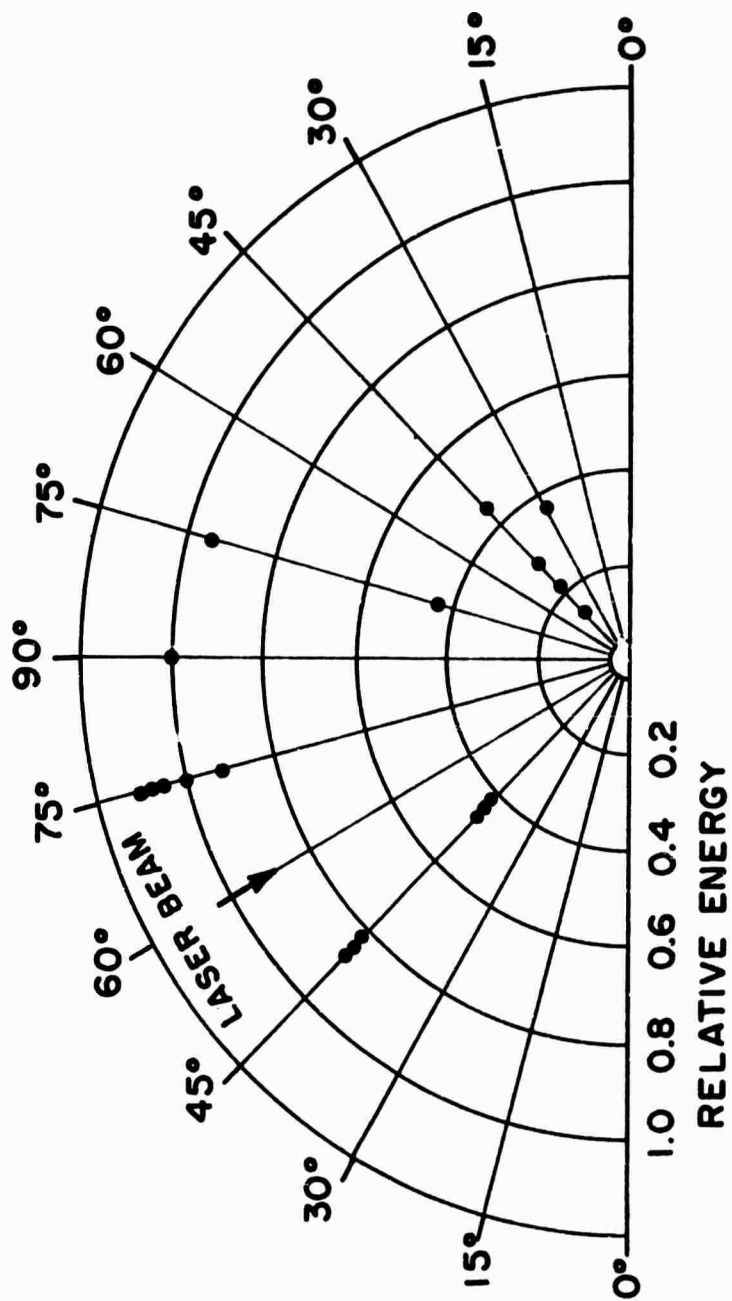


Figure II-13 - Ion Energy Distribution In Plane Containing Laser Beam
And Target Normal

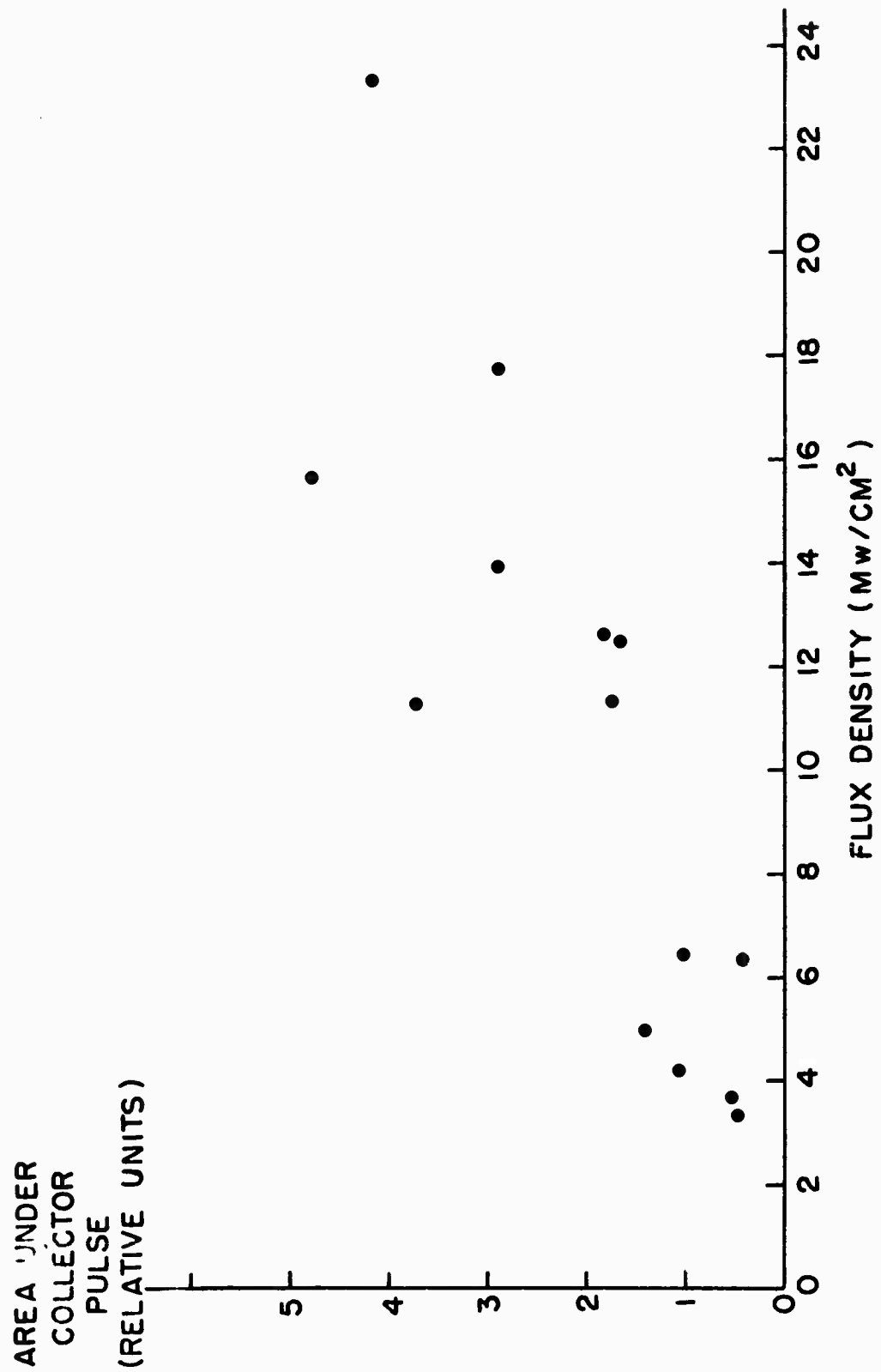


Figure II-14 - Ion Emission As Function Of Laser Power. Integrated Data From Collector Along Normal To Target.

D HIGH POWER LASER

In operating the new large ruby laser the output of the laser was raised as high as 200 megawatts. However, this resulted in damage to the ruby rod. The damage appears in the form of internal voids in the ruby. Some of these voids which scatter light in a transverse direction may be seen in Figure II-15. The photograph was taken with the beam of a helium-neon laser traveling down the ruby rod axis. A possible cause of this damage was filamentary laser action in the rod which occurred using the Q-switching dye which has the tendency to become transparent over small areas early in the pulse. This leads to a very non-uniform power distribution in the beam and local flux densities much higher than the average value can occur. This means that in small filaments in the rod the flux density is high enough to cause damage even though the average flux density over the face of the rod is well below the damage threshold. Photographs taken in a Twyman-Green interferometer substantiate this view.

Figure II-16 shows a Twyman-Green interferogram of the damaged rod. The rod appears as the roughly elliptical segment near the center of the picture. It appears this way because of the Brewster angle end faces. There are about four fringes across the rod diameter. The triangle in the upper left is a background reference. The damage is not spread out over the entire surface, but is localized in small regions across the cross-sectional area of the interferogram substantiating the view that the damage has occurred along filaments down the rod. Moreover, even after damage this rod was operable at levels of approximately 50 megawatts. This implied that it is only a portion of the rod which underwent the laser action at flux densities in excess of the threshold for damage.

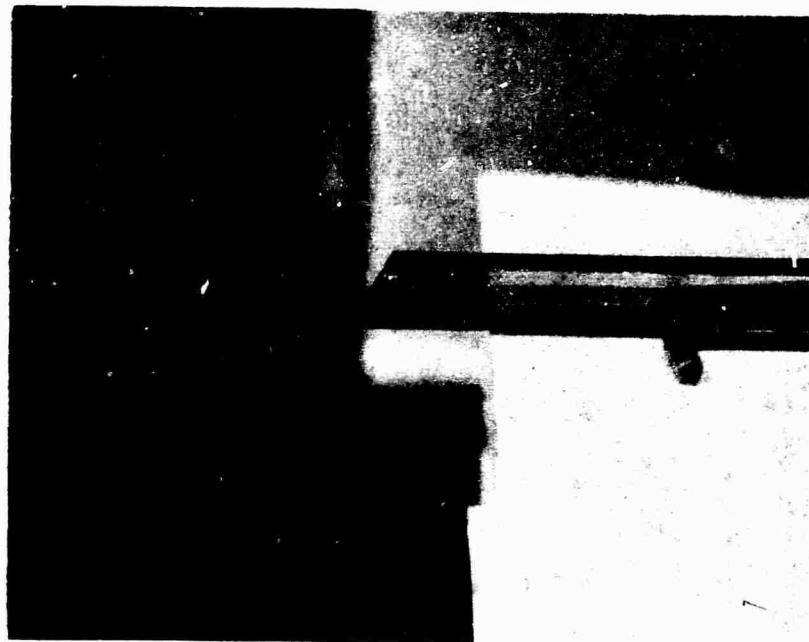


Figure II-15 - Scattering Centers In Damaged Ruby Rod



Figure II-16 - Twyman-Green Interferogram Of Damaged
Ruby Rod

A new six inch long ruby rod has been obtained from the Linde Corp. In using this new rod we shall be careful to monitor the laser pulses in order to avoid exceeding the level at which damage to the rod will occur. We have set up new monitoring procedures in which we have calibrated the amount of light received by a phototube after diffuse reflection from an MgO block. By keeping the entire output of the laser, integrated over the face, below approximately 100 megawatts, we should avoid exceeding the level at which damage occurs in the filaments. We shall also use a single cryptocyanine cell instead of two cells within the optical cavity since there is some evidence that filamenting action occurs more readily when there is a cryptocyanine cell at each end of the laser rod. Because of the noise problems in the hemispherical interaction chamber as noted above, when the flux density in the laser beam is high, we shall not be able to use this larger laser immediately to extend the range of powers in our measurements as we had originally planned to do.

SECTION III

THEORETICAL WORK

A. COMPARISON OF PULSE SHAPES WITH FREE EXPANSION

We have compared the pulse shapes obtained in the hemispherical chamber to the results predicted if the pulses arise from adiabatic free expansion of a high temperature plasma produced at the time of the laser pulse immediately in front of the target.⁽⁵⁾ These calculations were modified to give the flux as a function of time at a position 9.85 cm from the target, a distance equal to the radius of the hemisphere. Some results are shown in Figure III-1 for the asymptotic case of adiabatic free expansion of a plasma of mass 23 ions at a temperature of 200,000° K. This is compared to the observed pulse shape obtained from the collector along the normal to the target with zero voltage applied to the target. From earlier measurements^(1, 2) we deduced on the time of flight spectrometer than under these circumstances the sodium component gave the dominant contribution to the ion emission from the tungsten target. We see that the observed pulse shapes are similar in shape and in halfwidth. The predicted value from theory has a somewhat longer tail, but it may be that the tail of the experimentally determined pulse is lost at larger time values because of the difficulty in determining when the pulse has returned to the base line. Also, the earlier rise of the experimental pulse may be due to the arrival of a light component such as hydrogen. We find that the observed pulse shape is approximately half way between the calculated values for the asymptotic free expansion of a mass 23 plasma at 100,000° K and 200,000° K.

These results are in agreement with the model in which the blowoff material (at least the ions in it) is heated to ~ 20 ev and then expands, giving the observed pulse shapes. It agrees also with other experimental estimates of the temperature of the blowoff material, based on optical measurements, which appear to yield values of the order of 10^5 degrees under a variety of experimental conditions.^(6, 7, 8)

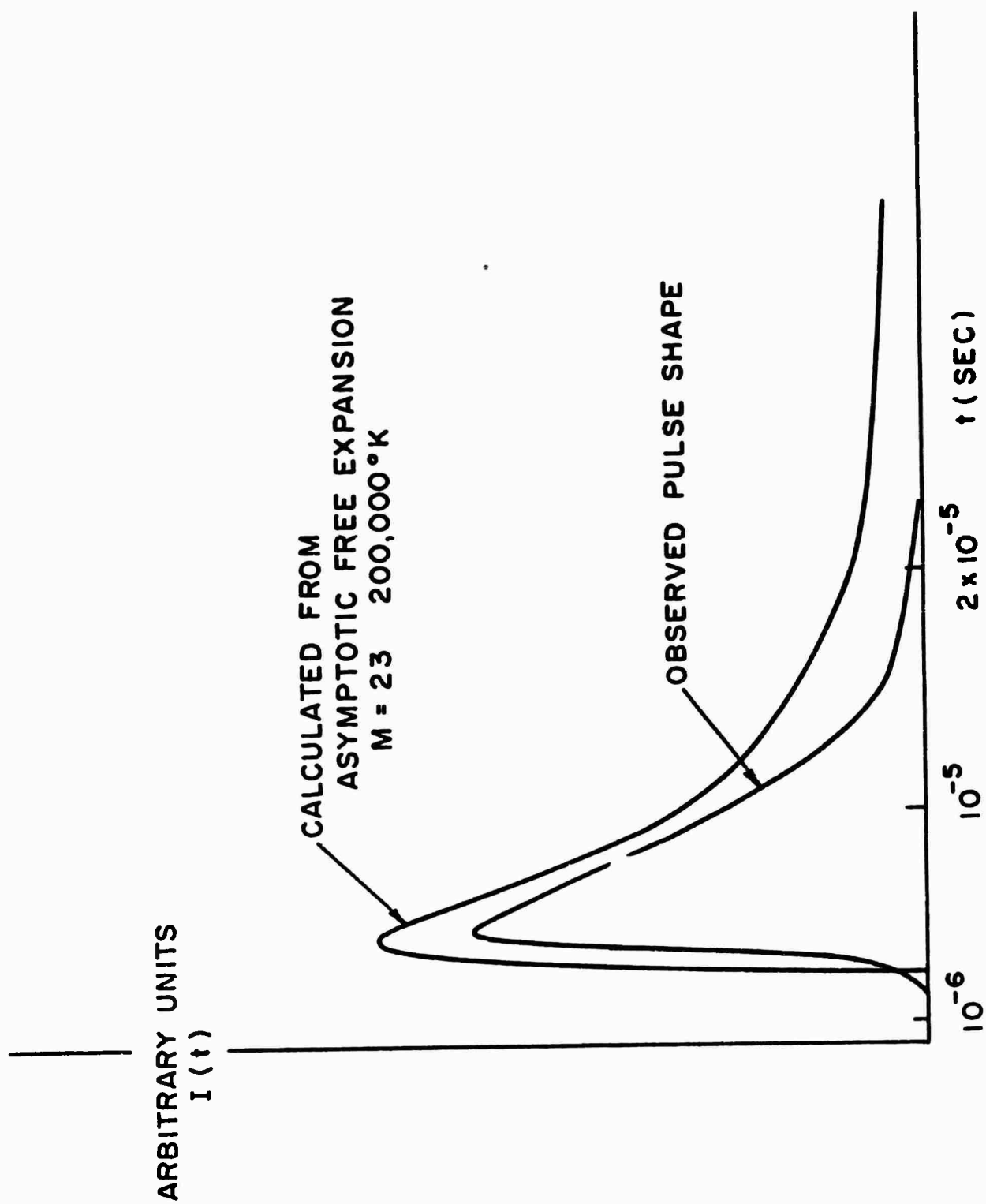


Figure III-1 - Pulse Shapes in Interaction Chamber

B. PLASMA HEATING

A recurring question in this work has been the role of heating the blowoff material by incoming laser radiation. At relatively high laser powers the heating rates can be high enough and the particle densities large enough that a considerable amount of radiation can be absorbed in the blowoff material and the production of high energy ions can be expected. The theoretical treatment appears to agree reasonably well with experimental results in the high power regime. However, at lower powers, around $50 \text{ megawatts/cm}^2$, there has been a problem in that the theoretical calculations indicate too low a rate of energy absorption to account for the experimental data. We analyzed the result for blowoff material consisting of neutral gases such as we observed in our quadrupole spectrometer, and concluded that heating by absorption of the laser radiation in an inverse Bremsstrahlung process in the neutral gas could not produce the observed results.⁽²⁾ Later we suggested an alternative hypothesis,⁽⁵⁾ namely that the absorption of radiation takes place mainly for electrons in the Coulomb field of alkali metal ions such as we have observed in the time of flight spectrometer. The electronic energy is transferred to the ions via Coulomb collisions but the energy is coupled relatively inefficiently to any neutral atoms which are present. This model results in an increased rate of heating at lower laser powers than if all heavy particles, atoms and ions, shared the available energy.

Earlier we described calculations of the adiabatic free expansion of a heated gas⁽⁵⁾ and in Section III-A of the present report we describe a comparison between these calculated results and the pulse shape observed in our interaction chamber. The agreement is quite good for expansion of a gas heated to approximately $200,000^\circ \text{K}$. This leads to a physically appealing picture of heating of the alkali metal ions in the blowoff material and subsequent free expansion of the alkali ions. However, this picture runs into difficulty when it is evaluated quantitatively.

The problem has been approached mathematically from two points of view. First there is a computer program which calculates heating and ionization of a sodium gas heated by absorption of laser radiation. The second approach has been to consider the heating process including equipartition of energy in the gas and the motion and spatial extent of the material. These two approaches are complementary. Neither represents the full problem, but each gives a different insight into it.

Let us consider the computer program first. In an ionized gas at temperature T the absorption coefficient for radiation of frequency ν is given by the following formula:

$$k_{\nu} = \frac{3.69 \times 10^8 n_e}{\nu^3 T^{1/2}} [1 - \exp(-h\nu/kT)] \sum_Z Z^2 N(Z) \log \Lambda \quad (1)$$

$$\text{where } \Lambda = \frac{3e^3}{2Z^2} \left(\frac{k^3 T^3}{\pi n_e} \right)^{1/2}$$

n_e = electron density, $N(Z)$ = density of atoms in ionization state Z , and the sum goes over all ionization states present in the gas.

From this absorption coefficient we get the rate of heating of the gas, assuming very rapid equipartition of the absorbed energy between the electrons and ions and neglecting gas expansion during the heating.

This treatment takes into account the fact that the rate of heating increases as the gas becomes more ionized. According to equation (1), as one increases the level of ionization from one to two, the heating rate should increase by a factor of four. Therefore, thermal ionization will increase

the heating rate, which in turn gives rise to more ionization in a process with regenerative feedback. The state of ionization of the gas was considered in the May, 1967 report⁽⁵⁾ and is described by Equation III-4 of that report. This represents a coupled set of Saha equations. One must first calculate the partition function $Z(T)$. To do this requires knowledge of the excited energy levels in each ionization state of the molecule. These are available for the first nine ionization states of sodium, that is, for sodium ionized eight times or less, in the NBS tabulation of energy levels.⁽⁹⁾ For the zeroth ionization state of sodium there are over 170 excited levels listed. Since each excited state enters with a weighting factor $\exp(-E_n/kT)$, where T is the temperature and E_n the energy of the n th level, this means an extremely large amount of computational work to calculate the partition function as a function of temperature, and thus the problem is suitable only for a computer.

A Runge-Kutta routine was written to calculate the heating rate of sodium gas absorbing radiant energy. At a given temperature, with the populations of the various states known, a heating rate was calculated from the absorption given by equation (1) and at a time increment later the new temperature was determined according to the Runge-Kutta formalism.⁽¹⁰⁾ At each intermediate step in the Runge-Kutta routine, the partition functions for the intermediate temperature were calculated for each ionization level of sodium in a subroutine and the coupled set of Saha equations was solved to adjust the populations of the various ionization states to the new temperature. The electron density was calculated at each step, and the change in the ionization potential due to the Coulomb interaction as described in the May, 1967 report⁽⁵⁾ was also calculated. The correction to the ionization potential was large enough so that for each ionization state of sodium enough

energy levels were given in the NBS tables⁽⁹⁾ so that the highest value of E_n given exceeded the corrected ionization potential. Thus we did not have to be concerned about having a region in which there would be a large number of unknown energy levels slightly below the ionization potential. The computer routine was run on the Honeywell H-1800 computer for various choices of input power and initial sodium density. The starting temperature was taken to be 5000°K, roughly characteristic of the tungsten surface heated by the laser, but results are not critically dependent on the initial temperature. At 5000°K sodium is almost entirely singly ionized.

We had expected that by including only the alkali ions in the system, rapid and effective heating would occur, particularly when we allowed for the possibility of multiple ionization of the alkali ions. The results indicated that heating is indeed possible at lower particle densities than were indicated by the results of the similar method as described in the December, 1965 report.⁽²⁾ Results of the computer programs for various initial conditions are shown in Figure III-2. The laser pulse was taken as constant in time with duration equal to 30 nanoseconds. The various curves represent different initial conditions of particle density and laser flux density. Curve a represents sodium density of 10^{16} cm^{-3} and laser flux density of 10^8 watts/cm^2 . Curve b is for 10^{17} cm^{-3} and 10^8 watts/cm^2 . Curve c is for 10^{18} cm^{-3} and 10^8 watts/cm^2 . Curve d is for 10^{18} cm^{-3} and $3 \times 10^8 \text{ watts/cm}^2$. Curve e is for 10^{18} cm^{-3} and 10^9 watts/cm^2 . These results show that heating can occur at particle densities at least an order of magnitude lower than indicated by the earlier model in which neutral gas was also coupled into the absorbing system.⁽²⁾ However, the results still indicate the requirement for high laser powers and high particle densities to cause heating. The numbers are too high to be realistic for our system. We would estimate, from measurements of the total number of sodium ions in the time of flight spectrometer and the thermal

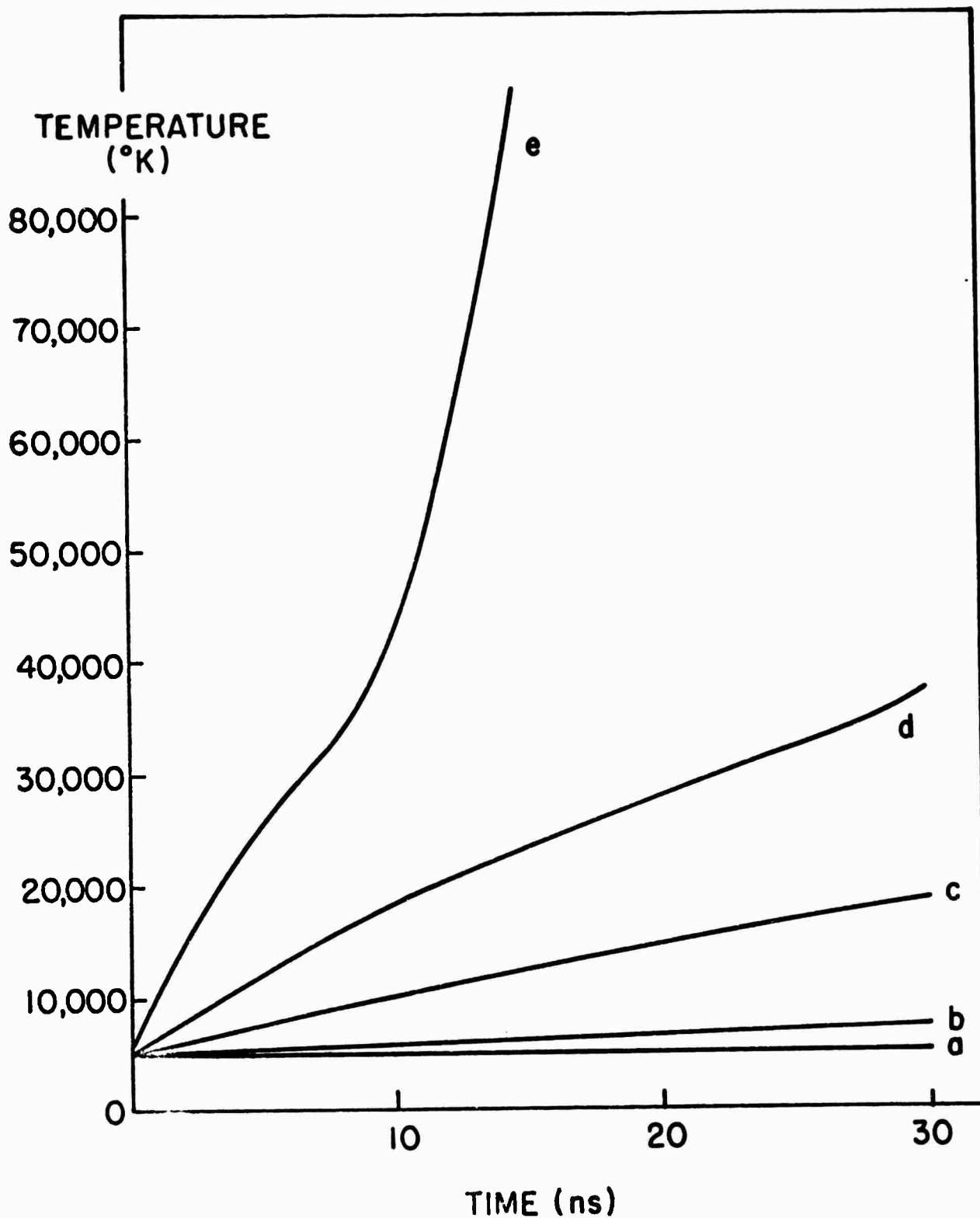


Figure III-2 - Calculated Temperature in Plasma Heating Model. Initial Conditions:

N_a = sodium atom density, I_o = laser flux density

Curve a: $N_a = 10^{16} \text{ cm}^{-3}$, $I_o = 10^8 \text{ w/cm}^2$

Curve b: $N_a = 10^{17} \text{ cm}^{-3}$, $I_o = 10^8 \text{ w/cm}^2$

Curve c: $N_a = 10^{18} \text{ cm}^{-3}$, $I_o = 10^8 \text{ w/cm}^2$

Curve d: $N_a = 10^{18} \text{ cm}^{-3}$, $I_o = 3 \times 10^8 \text{ w/cm}^2$

Curve e: $N_a = 10^{18} \text{ cm}^{-3}$, $I_o = 10^9 \text{ w/cm}^2$

velocity of the ions emitted from the tungsten surface during the time of the laser pulse, that a density around 10^{13} to 10^{14} sodium ions/cm³ would be more likely in our experimental conditions. However, the results are interesting in that they indicate the conditions under which plasma heating can occur. It is worthwhile to consider the calculated results in some detail.

There are some noteworthy points to make about the details of the various computational runs. The first point concerns curve e in Figure III-2, in which conditions for a runaway heating occur. At the end of 30 nanoseconds the computed temperature has risen above 400,000° K. This is probably unrealistic since, as the material gets very hot, it would expand rapidly and the losses would limit the temperature rise. Indeed it is very likely that the approximately constant value of 100,000 to 200,000° K for the temperature of the blowoff material, as observed in different experimental conditions, may indicate the level at which losses from the high rate of expansion and losses by radiation become large enough to cut off the heating. Thus, the potential for heating by this mechanism is more than adequate to account for the experimentally observed energies if the particle density is high.

Another point worth mentioning about curve e in Figure III-2 is that a high enough temperature is calculated so that the system would reach ionization states higher than eight times ionized sodium. These higher ionization states are cut off artificially by the computer routine since we do not have the available input data for the energy levels of the higher ionized states. Thus at the end of the computation we are in a physically unrealistic situation in that the material is prevented from ionizing to the level to which it would if a temperature of 400,000° K were actually attained. The shapes of the curve are also interesting. At times less than about eight nanoseconds the curve is concave downward. This occurs

because of the form of equation (1) which indicates that the absorption coefficient decreases with increasing temperature because of the $T^{1/2}$ term in the denominator, so long as the ionization state does not change appreciably. When the temperature reaches about 30,000° K, doubly ionized sodium becomes an appreciable fraction of the total. When this occurs, the heating rate increases rapidly and the curve becomes concave upward. A slight upward concavity may also be noted just at the end of curve d where a temperature of approximately 35,000° K and a considerable fraction of doubly ionized sodium is reached near the end of the laser pulse.

The calculated results for the fractions of the various ionization states are of interest. Figure III-3 shows the results for an initial density of 10^{18} cm^{-3} and a flux density of 10^8 watts/cm^2 , i. e., for the same case as curve c. The material remains almost entirely singly ionized throughout the 30 nanosecond pulse duration even though the temperature is calculated to rise to over 18,000° K. The material is practically all singly ionized, but the fraction of un-ionized material rises throughout the time duration of the pulse. This is somewhat surprising at first in that we would expect the fraction of un-ionized material to decline. The increase occurs because of many excited states of un-ionized sodium that lie at relatively low levels, below 35,000 wave numbers. Therefore, as these excited states become accessible as the temperature rises, the partition function of the un-ionized state becomes large and the relative weight of this state causes the rise as shown in Figure III-3. Just at the end of the laser pulse we can see that the doubly ionized sodium is just coming on to this scale.

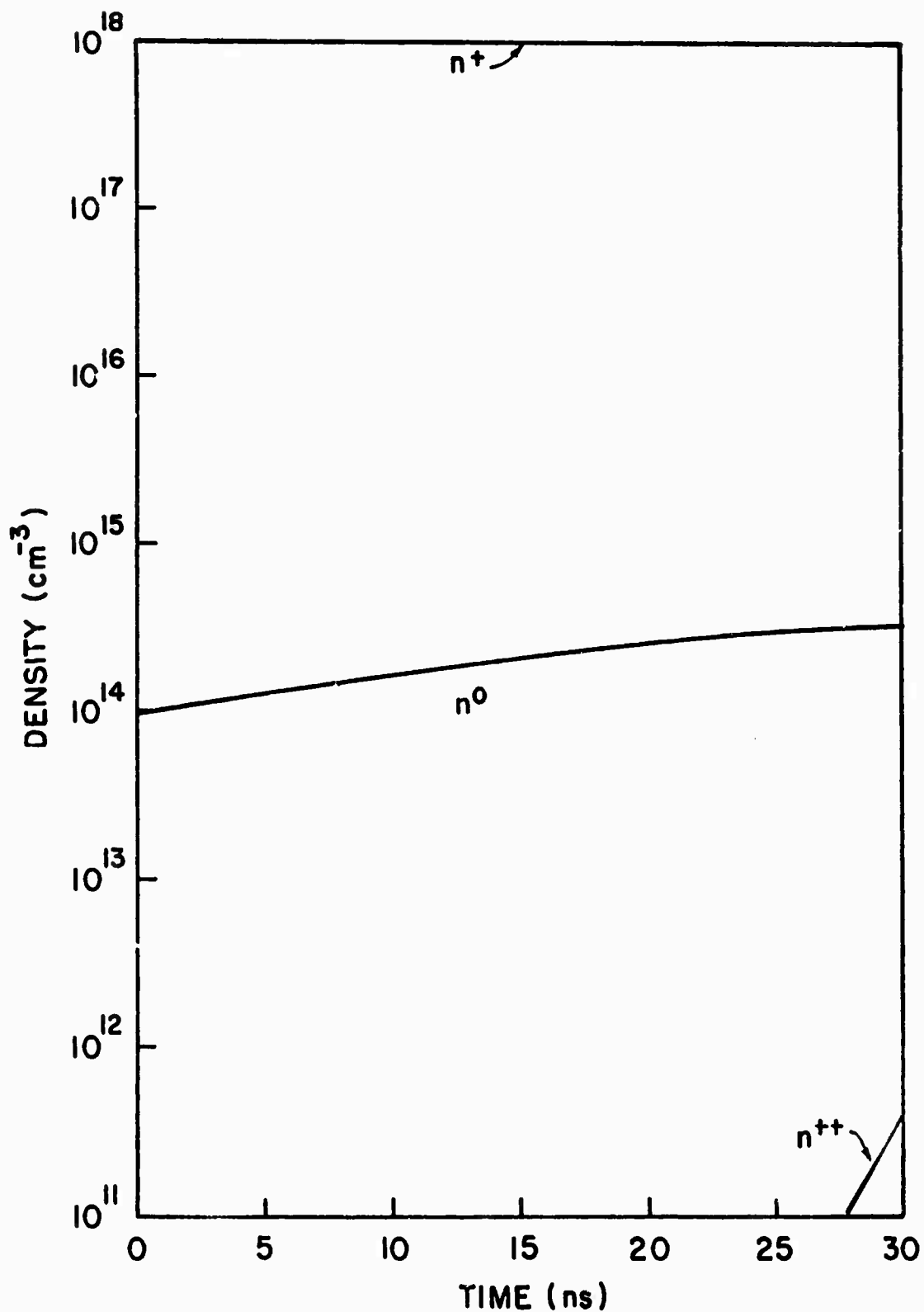


Figure III-3 - Densities for Various Ionized States of Sodium as Calculated on Plasma Heating Model as Functions of Time. Initial Sodium Density:

10^{18} cm^{-3} ; laser flux density: 10^8 W/cm^2

In Figure III-4 we see the result for the case of 10^{18} cm^{-3} and a flux density of $3 \times 10^8 \text{ watts/cm}^2$, i. e., for the same case as curve d. At approximately 25 nanoseconds, where the temperature of the material has risen to approximately $30,000^\circ \text{K}$, doubly ionized sodium has reached approximately ten percent of the total. Triply ionized sodium comes on to the scale at a low level near the end of the pulse. Un-ionized sodium rises to a broad peak because of the increase in the partition function as mentioned before and then begins to decline as the doubly ionized sodium begins to account for an appreciable fraction of the material.

In Figure III-5 we see the results for the case in which we have runaway heating to a very high level, i. e., for the case of an initial density of 10^{18} cm^{-3} and 10^9 w/cm^2 , the same as curve e. This curve is cut off at approximately 23 nanoseconds because at this point almost all the sodium is eight times ionized. In physical reality we would at this point have nine times ionized sodium coming into dominance as a large fraction of the total number. However, our computer program has no input data to account for nine times ionized sodium, and therefore cannot realistically account for this phenomenon. Therefore we do not present the results at times greater than 23 nanoseconds. We see that the behavior is qualitatively as follows. Singly ionized sodium dominates for about the first eight nanoseconds. At 11 nanoseconds when the temperature would be approximately $50,000^\circ \text{K}$, doubly ionized sodium reaches its peak and begins to drop off. Triply ionized sodium reaches a peak around 14 nanoseconds when the temperature would be approximately $80,000^\circ \text{K}$. Four times ionized sodium dominates at around $100,000^\circ \text{K}$. Near $150,000^\circ \text{K}$ (18 nanoseconds) five times ionized sodium is largest. At $200,000^\circ \text{K}$ (20 nanoseconds) seven times ionized sodium is largest. At $273,000^\circ \text{K}$ (approximately $22\frac{1}{2}$ nanoseconds), eight times ionized sodium becomes the largest factor. The curves represent the behavior of the solutions of the coupled set of Saha equations III-4 of the May, 1967 report⁽⁵⁾ as the temperature increases.

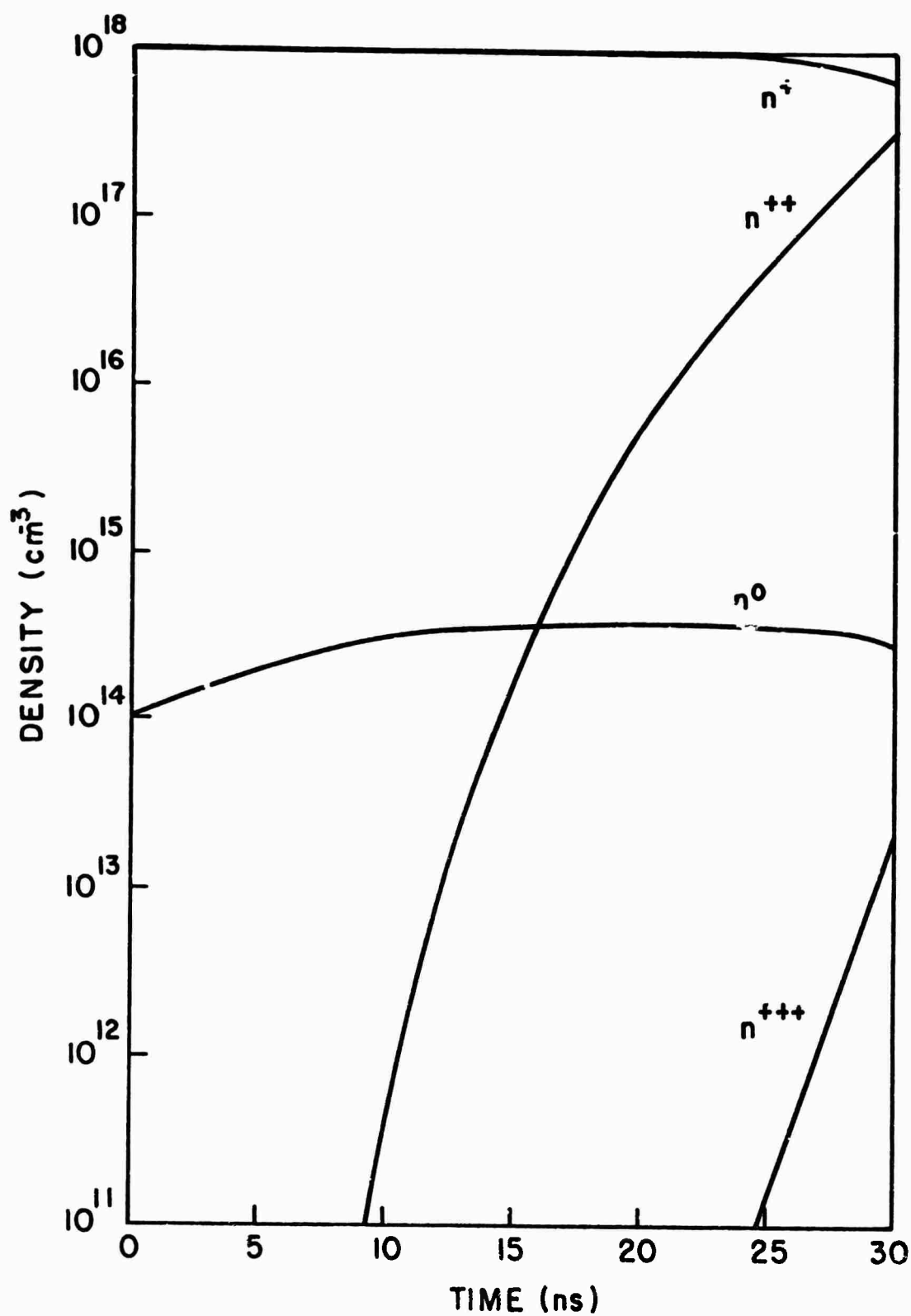


Figure III-4 - Densities for Various Ionized States of Sodium as Calculated on Plasma Heating Model as Functions of Time. Initial Sodium Density: 10^{18} cm^{-3} ; laser flux density: $3 \times 10^8 \text{ w/cm}^2$

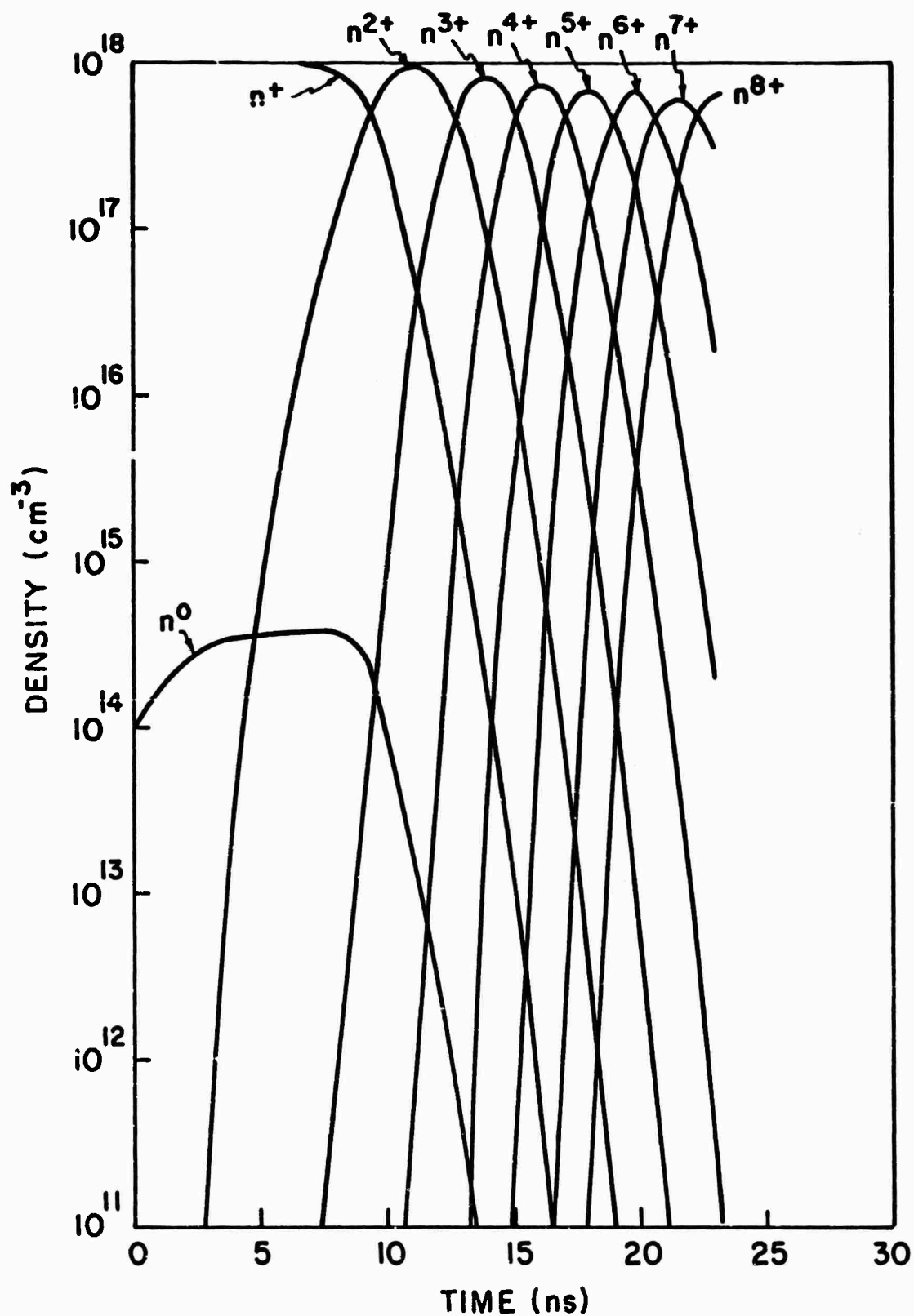


Figure III-5 - Densities for Various Ionized States of Sodium as Calculated on Plasma Heating Model as Functions of Time. Initial Sodium Density: 10^{18} cm^{-3} ; laser flux density: 10^9 w/cm^2

The results have the following implications. If we do indeed heat the blowoff material to approximately $100,000^\circ\text{K}$, we should have an appreciable fraction of three, four, and five times ionized sodium. We have not detected these species in our experimental system. This means that they must either recombine very fast or the temperature does not become this high. It is plausible that even if these species are produced they could recombine so fast that they would not be observed in the time of flight spectrometer measurements. They should, however, be detectable by optical emission lines. Fawcett, for example, has in his laser-produced plasmas seen lines of 13 times ionized calcium and titanium.⁽¹¹⁾

Thus, on the basis of this analysis, we conclude that the conditions for runaway heating to temperatures of the order of $100,000^\circ\text{K}$ are that the sodium ion density should be approximately 10^{18} cm^{-3} and laser flux density approximately 10^9 watts/cm^2 . We could postulate the possibilities of nonuniformity in either the laser power or in the sodium density as, for example, would be expected in the tungsten. This would give rise to a local very high concentration of sodium ions. However, these hypotheses are rather unsatisfactory and it must be concluded at the present time that there are grave difficulties in the quantitative evaluation of this model in which we evaluate the possible heating of the blowoff material.

The study of the plasma heating problem so far indicates the importance of the plasma density. Unfortunately direct information on the plasma density is not available and we are therefore forced to leave plasma density as an independent variable or construct a model of the emission process and estimate it. In what follows we will attempt to construct a useful model.

In the treatment described before we neglected many important points about the processes occurring in the blowoff material. In particular we neglected any motion of the material and also considered the equipartition of energy between electrons and sodium ions to be instantaneous. Including

these factors would lower the calculated heating rate, so that the earlier results give an overestimate. We will attempt to introduce the particle density in a more natural way, instead of simply allowing it to be an independent variable.

The following development will consider some of these points. In so doing we make many assumptions which will appear later. Thus, the treatment is limited by these restrictions. We do not allow the realistic representation of the increasing ionization with increasing temperature as we did before, but consider only one ionic species. The result is subject to the stated assumptions, but does give a different perspective into the problem.

We assume that sodium is emitted from the target surface singly ionized. Any atomic or molecular material (including atomic sodium) will not be considered as part of the system because of the long time scale for transfer of energy to these neutrals.

The process considered is the heating of the electrons by inverse Bremsstrahlung and the subsequent transfer of energy to the ions by collisions. Only one spatial dimension and one ion species are considered.

In this calculation we approximate the time variation in laser power and target temperature, but the spatial variations are ignored. The laser pulse is assumed to have the simple form.

$$\begin{aligned}
 P_{\ell} &= P_m t/t_m & t \leq t_m \\
 &= P_m (2 - t/t_m) & t_m \leq t \leq 2t_m \\
 &= 0 & t \geq 2t_m
 \end{aligned} \tag{2}$$

where P_{ℓ} and P_m are the instantaneous and peak laser flux densities and t_m is the time at which laser power is maximum. When we speak of "laser

power" we normally mean average (over some area) peak (in time) power. The appropriate value of P_m for the calculation may be somewhat higher than this average peak power.

As an approximation to the real case, it will be assumed that the instantaneous target temperature is proportional to the instantaneous laser power density. In earlier work ⁽¹²⁾ we estimated that for tungsten targets the average peak temperature in °K is approximately 60 times the average peak laser flux density in megawatts/cm² for a 30 ns duration laser pulse. The target temperature is then given by

$$\begin{aligned}\theta_T &\approx 60 \times 10^{-6} \frac{kP_\ell}{e} \\ &\approx 5 \times 10^{-9} P_\ell\end{aligned}\tag{3}$$

where θ_T is the target temperature in electron volts and P_ℓ is the laser flux density in watts/cm², and we take $e\theta_T$ to be of the order of kT , where T is the temperature in °K.

By making assumptions concerning the rate of ion emission and the velocity of the particles, an expression for plasma density as a function of time can be obtained.

We assumed that the X-component of velocity of the ions equals the average velocity of the half-Maxwellian distribution corresponding to the target temperature at the time of emission.

$$v_x = \frac{1}{2} \left(\frac{2kT}{M\pi} \right)^{1/2}\tag{4}$$

where M is the ion mass. From this point on, the analysis will be restricted to the first half of the laser pulse. Any increase in velocity due to the plasma heating during the first half of the laser pulse will be neglected.

At time $t < t_m$, the average velocity of ions emitted τ seconds earlier is found by substituting equations (2) and (3) into equation (4).

$$v_x(t, \tau) = \left[\frac{6 \times 10^{-5} k}{2 \pi M} \frac{P_m(t - \tau)}{t_m} \right]^{1/2} \quad (5)$$

and the position of these ions is given by:

$$x(t, \tau) = v_x(t, \tau) \tau \quad (6)$$

To find the extent, x_{\max} of the plasma at the time t , equation (6) may be differentiated with respect to τ and the result set equal to zero. By substituting equation (5) into equation (6) and carrying out the differentiation it is found that x is maximum when $\tau = 2t/3$, or

$$x_{\max} = \frac{2}{3\sqrt{3}} \left(\frac{6 \times 10^{-5} k}{2 \pi M} \right)^{1/2} \left(\frac{P_m}{t_m} \right)^{1/2} t^{3/2} \quad (7)$$

Unfortunately the history of the ion emission during the laser pulse is not known. A crude approximation will be used here and then the effects of the approximation will be considered at the end of the analysis.

It will be assumed that the ions are emitted continuously from time $t = 0$ at a rate proportional to the target temperature. Because of the assumed time dependence of the target temperature:

$$\Gamma_i = \Gamma_m t/t_m \quad (8)$$

for $t < t_m$ and where Γ_i and Γ_m are instantaneous and the peak ion emission flux densities respectively. In order to relate the result to quantities which can be inferred from experimental observations, it is assumed that

$$\int_0^{t_m} \Gamma_i dt = N_T/2 \quad (9)$$

where N_T is the total number of ions/cm² emitted from the target during the laser pulse. It is easily shown that

$$\Gamma_m = N_T/t_m \quad (10)$$

Now the average ion density will be

$$n_i = \frac{1}{x_{\max}} \int_0^t \Gamma_i dt \quad (11)$$

Upon making the appropriate substitutions, for $M = 23$ times the proton mass,

$$\begin{aligned} n_i &= N_T t^{2/2} x_{\max} t_m^2 \\ &= \frac{3 \sqrt{3}}{4} \left(\frac{2\pi M}{6 \times 10^{-5} k} \right)^{1/2} \frac{N_T t^{1/2}}{P_m^{1/2} t_m^{3/2}} \\ &= \frac{0.22 N_T t^{1/2}}{P_m^{1/2} t_m^{3/2}} \end{aligned} \quad (12)$$

In the absence of laser heating, the average electron and ion temperatures θ_e and θ_i would be:

$$\theta_i = \theta_e = \frac{\int_0^t \Gamma_i \theta_T dt}{\int_0^t \Gamma_i dt} \quad (13)$$

and under the stated assumptions

$$\theta_i = \theta_e = 2 (\theta_T)_{\max} t / 3 t_m \quad (14)$$

For convenience we have used the average densities and temperatures. Local densities and temperatures will of course be different.

The absorption of laser energy is assumed to occur through the inverse Bremsstrahlung process and is taken to be described by the expression given by Spitzer. ⁽¹³⁾ The absorption coefficient is given as

$$k_\nu = \frac{3.69 \times 10^8 Z^3 n_i^2}{T^{1/2} \nu^3} g_{ff} \left[1 - \exp(-h\nu/kT) \right] \text{ cm}^{-1} \quad (15)$$

where g_{ff} is a correction factor "normally" near unity and will be taken as such in this calculation. (Whether or not the situation under consideration is "normal" has not been examined in detail.) This differs from the absorption coefficient used in the computer program in that here we consider one ionic species to be dominant. Inserting the numbers and symbols appropriate to this analysis, the absorption coefficient is:

$$k_\nu = 4.25 \times 10^{-38} Z^3 n_i^2 \theta_e^{-1/2} \left[1 - \exp(-1.8/\theta_e) \right] \text{ cm}^{-1} \quad (16)$$

The rate of increase of electron temperature due to absorption is given by

$$\frac{d\theta_e}{dt} = \frac{P_{\ell} k_v}{n_e e}$$

Ions will be heated by collisions with energetic electrons according to the equation

$$\frac{d\theta_i}{dt} = \frac{\theta_e - \theta_i}{t_{eq}} \quad (18)$$

$$\text{where } t_{eq} = \frac{5.87 A_e A_i}{n_i Z^2 \ln \Lambda} \left(\frac{T_i}{A_i} + \frac{T_e}{A_e} \right)^{3/2} \quad (19)$$

t_{eq} is the equipartition time for energy transfer⁽¹³⁾ and A_i and A_e are respectively the atomic mass numbers of the ions and electrons. For the system under consideration, $A_i = 23$, $A_e = 1/1837$,

$$t_{eq} \approx 7.2 \times 10^9 \theta_e^{3/2} / Z^2 n_i \ln \Lambda \quad (20)$$

where $\ln \Lambda$ is the factor as defined by Spitzer⁽¹³⁾, approximately equal to 10 under a wide variety of conditions.

The various terms can be collected to obtain one equation for electron heating.

$$\frac{d\theta_e}{dt} = \frac{2(\theta_T)_{\max}}{3 t_m} + \frac{P_{\ell} k_v}{e n_e} - \frac{\theta_e - \theta_i}{t_{eq}} \quad (21)$$

The first term on the right is due to the mixing of the hotter ions as the target heats up (obtained by differentiating equation 14), the second term is the laser absorption, the third represents the transfer of energy to the ions.

The ion heating may be expressed by

$$\frac{d\theta_i}{dt} = \frac{2(\theta_T)_{\max}}{3t_m} + \frac{(\theta_e - \theta_i)}{t_{eq}} \quad (22)$$

Substitutions from the preceding analysis can be made into the above equations with the result

$$\begin{aligned} \frac{d\theta_e}{dt} = & \frac{10^{-8} P_m}{3t_m} + \frac{3.06 \times 10^{-10} N_T t^{1/2} Z^2}{P_m^{1/2} t_m^{3/2} \theta_e^{1/2}} \\ & \cdot \left\{ 1.87 \times 10^{-10} \frac{P_m t}{t_m} [1 - \exp(-1.8/\theta_e)] + \frac{\theta_i}{\theta_e} - 1 \right\} \end{aligned} \quad (23)$$

$$\frac{d\theta_i}{dt} = \frac{10^{-8} P_m}{3t_m} + \frac{3.06 \times 10^{-10} Z^2 N_T t^{1/2} (\theta_e - \theta_i)}{P_m^{1/2} t_m^{3/2} \theta_e^{3/2}} \quad (24)$$

These two equations are in terms of given parameters P_m , t_m , N_T , and the unknowns θ_e , θ_i , and Z . The appearance of the average ionic charge Z considerably complicates the solution of these equations since it can be evaluated only by the use of the Saha equations as discussed previously. (5) While the simultaneous solution of the equations of this analysis could be carried out, let us first look at an approximation.

The maximum electron heating rate would be near $t = t_m$. An approximation to equation (23) at $t = t_m$ would be, assuming no significant heating up to that point:

$$\begin{aligned} \left(\frac{d\theta_e}{dt} \right)_{t=t_m} &\approx \frac{3.06 \times 10^{-10} N_T Z^2 \times 1.87 \times 10^{-10} P_m}{P_m^{1/2} t_m (5 \times 10^{-9} P_m)^{1/2}} \\ &\approx 8.1 \times 10^{-16} N_T Z^2 / t_m \end{aligned} \quad (25)$$

This result is interesting in that the laser power does not appear explicitly. One would expect, however, that the value of N_T observed in an experiment would be higher for higher laser power and thus higher heating rates could be expected.

To explain the observed plasma heating on the basis of this model, $d\theta_e/dt$ would have to have a value of the order of 10^9 (1 eV/nanosecond). For the experiment $t_m \approx 15 \times 10^{-9}$. If $Z \approx 1$, then from equation (25),

$$N_T \approx 2 \times 10^{16} \text{ sodium ions/cm}^2 \quad (26)$$

i. e., this is the value of N_T for which heating would occur. The experimental estimates for the number of ions involved in the heating process are about 10^9 ions⁽²⁾. If they are emitted from an area as small as 10^{-2} cm^2 we obtain a value of N_T about 10^{11} ions/cm² - five orders of magnitude too low to explain the heating.

Of the various approximations used in the analysis, the one regarding the ion emission rate is probably the least satisfactory. If the ion emission were more like a step function or a delta function originating at a certain target temperature, the all important plasma density would be higher. A more realistic approximation would be that the emission is an exponential function of temperature. Most of the emission would then occur in the time interval just before $t = t_m$ and the plasma density would be larger. However,

the result would be critically dependent on an activation energy which would not be well known. It is unlikely that the large discrepancy by several orders of magnitude could be resolved in this fashion.

In order to compare the second analysis with the first one contained in this report it should be of interest to calculate what plasma densities are predicted. Taking $N_T = 2 \times 10^{16}$, $P_m = 10^8$, $t_m = 1.5 \times 10^{-8}$, then equation (12) predicts a plasma density at the peak of the laser pulse of $3 \times 10^{19} \text{ cm}^{-3}$. This is not inconsistent with the other result. Using the experimental value of $N_T = 10^{11}$ would lead to $n_i = 1.5 \times 10^{14} \text{ cm}^{-3}$.

The equipartition time is also of interest. For the conditions assumed in this model, and for the experimentally derived values as in the preceding paragraph, equation (20) predicts an equipartition time of approximately 10^{-7} seconds. The observed ion heating would require an equipartition time nearly two orders of magnitude shorter. Again the plasma density is the dominant quantity, a higher density would yield a shorter equipartition time.

Thus on the basis of the suggested model⁽⁵⁾, the results of the two different approaches, although the assumptions are much different, are qualitatively similar in suggesting that the experimental value of the ion density is too low to account for heating of the ions in the blowoff material to temperatures of the order of 20 eV by absorption of the laser radiation.

C. PRESSURE PULSES

In the May, 1967 report⁽⁵⁾ we described results of calculations using the PUFF computer code to calculate the thermomechanical stress profiles produced in tungsten targets irradiated with laser radiation in 30 nanosecond pulses. The result typically involved propagation of short sharp stress waves with amplitudes of the order of $6 \times 10^8 \text{ dynes/cm}^2$ into the tungsten

target. These calculations have been extended to nickel and carbon target materials. The method is exactly the same as described in the May, 1967 report. Some results are shown in Figures III-6 and III-7 for the stress as a function of depth in a 50 micron thick nickel target at various times after the start of the laser pulse. Results are qualitatively very similar to those obtained from tungsten targets. The peak stress is approximately 6×10^8 dynes/cm² for a total energy deposition of 0.3 cal/cm². A compression wave is produced in the early stages of the energy deposition. The compression wave travels to the right and is reflected off the free back surface of the target as a rarefaction wave traveling to the left. A gradual attenuation of the amplitude of the wave may easily be seen. On each reflection from the surface of the target there is 180° change in the phase of the wave. The peak stress produced can be high, of the order of 600 atmospheres, but this is less than the yield strength of the metallic specimen so that we expect no permanent deformation of the material to result.

Similar results for carbon targets are shown in Figures III-8 and III-9. In these figures we see the gradual buildup of the amplitude of the original compression wave, and the start of travel of the peak amplitude toward the right. The peak amplitude in this case is reached after approximately half a nanosecond at a value of approximately 0.9×10^8 dynes/cm².

Because of the different mechanical properties of carbon, the amount of computer time required to run through a cycle in the PUFF code and to cover a given increment of problem time becomes unduly large and this calculation was cut off before the pressure wave reached the rear surface of the carbon. We would, however, expect the reflection properties of this wave to be exactly analogous to those of the other materials.

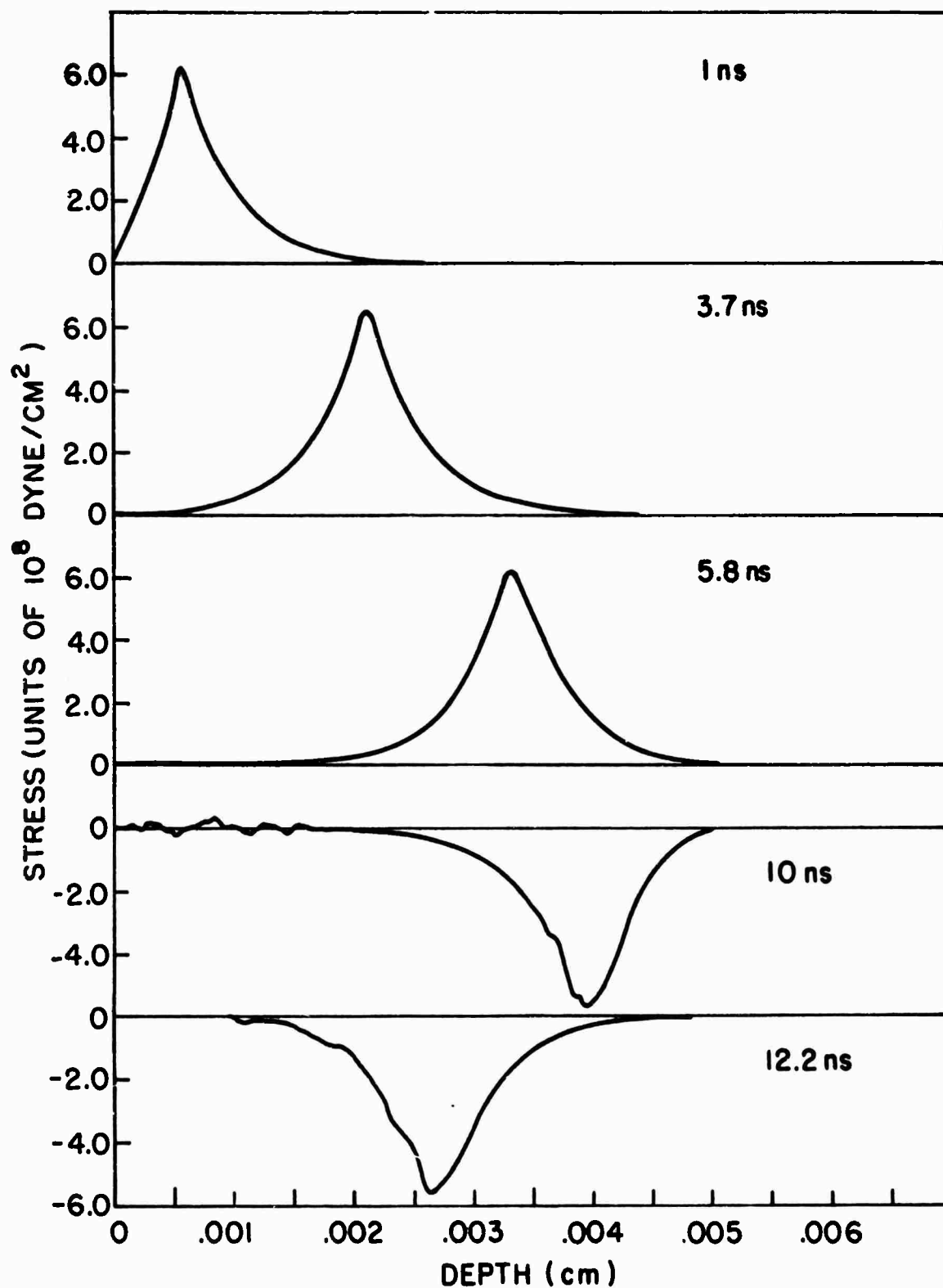


Figure III-6 - Stress Profiles in 50 Micron Thick Nickel Target as Calculated Using PUFF Code for Laser Pulse Depositing 0.3 cal/cm^2

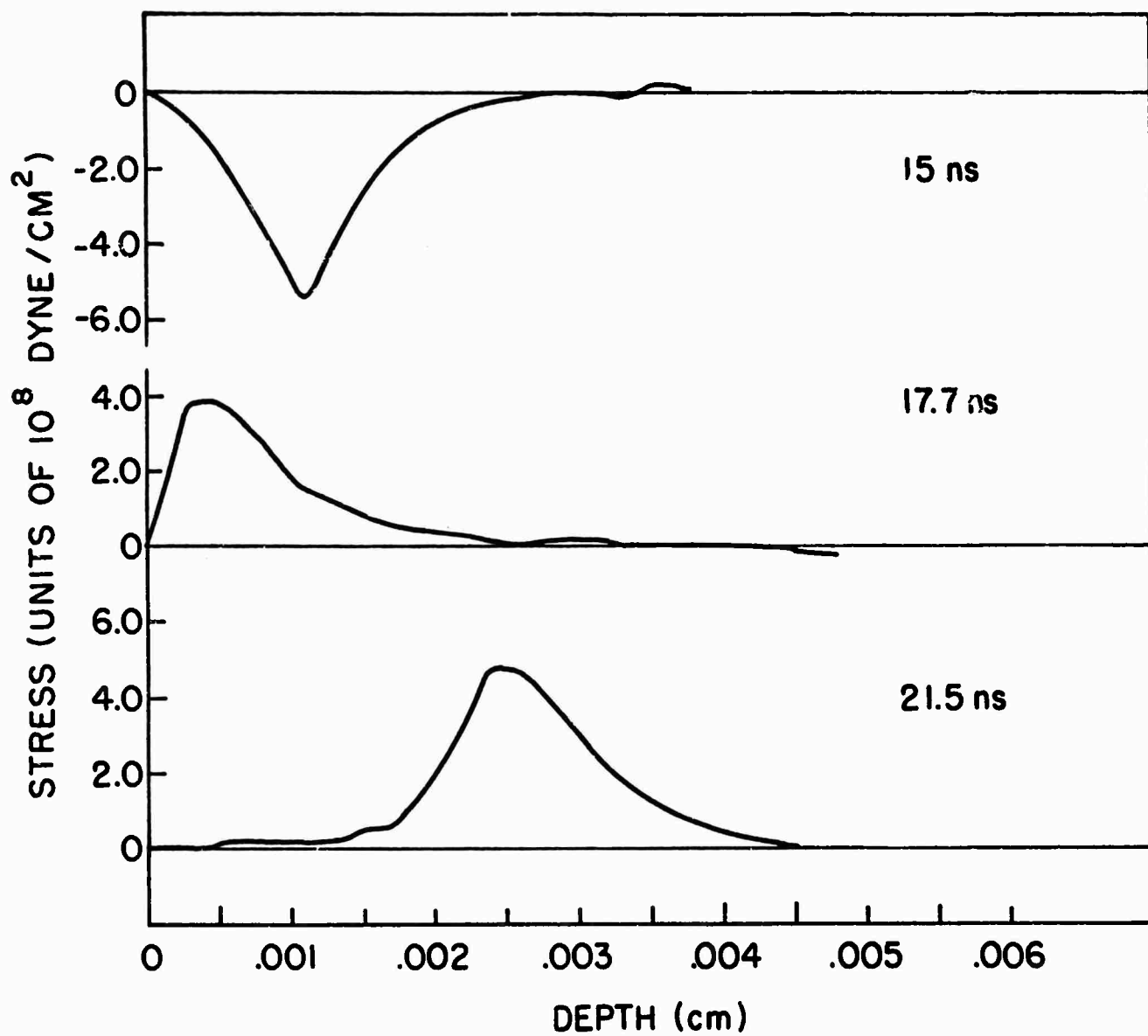


Figure III-7 - Stress Profiles in 50 Micron Thick Nickel Target as Calculated Using PUFF Code for Laser Pulse Depositing 0.3 cal/cm²

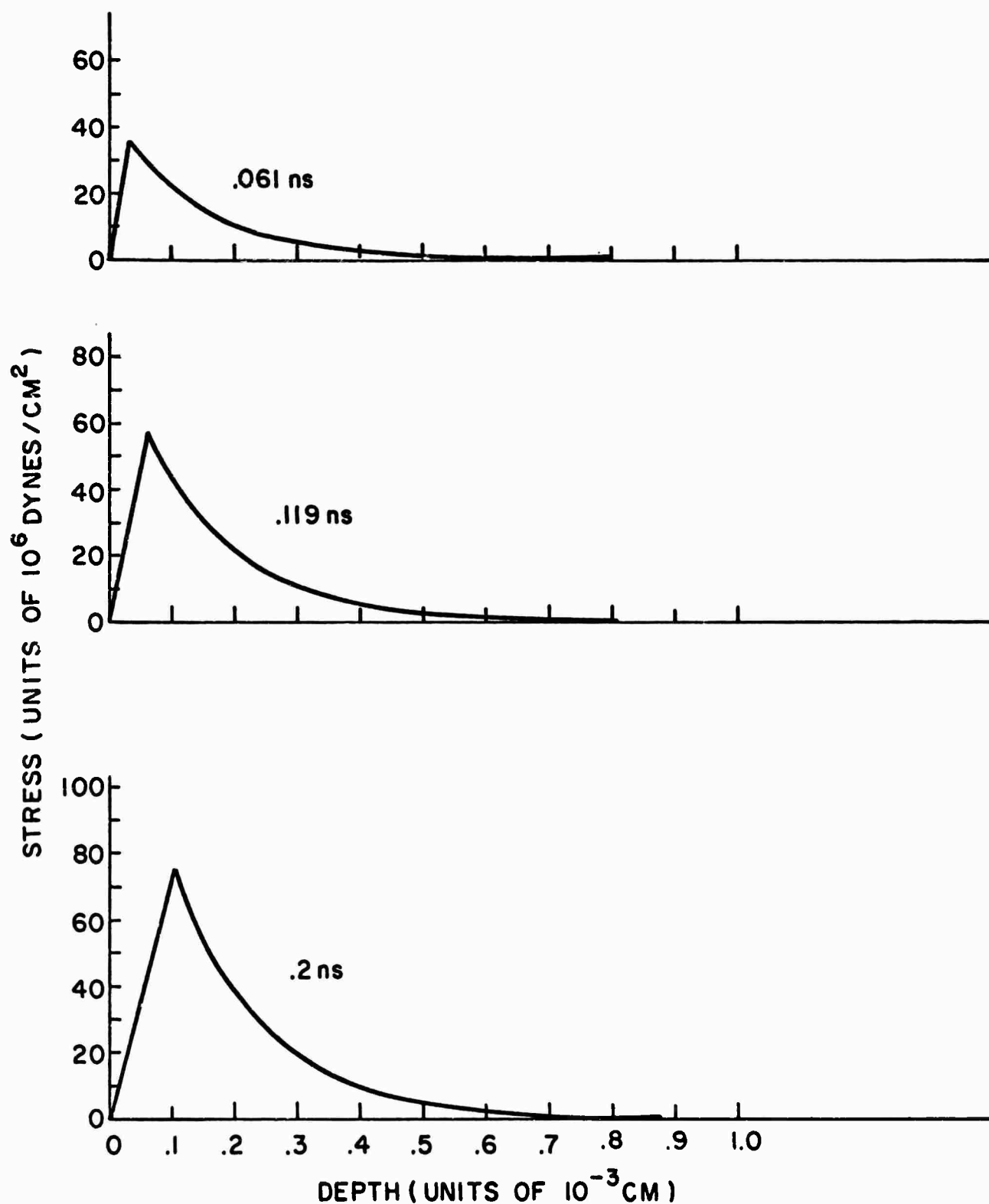


Figure III-8 - Stress Profiles in Carbon Target as Calculated Using PUFF Code for Laser Pulse Depositing 0.3 cal/cm^2

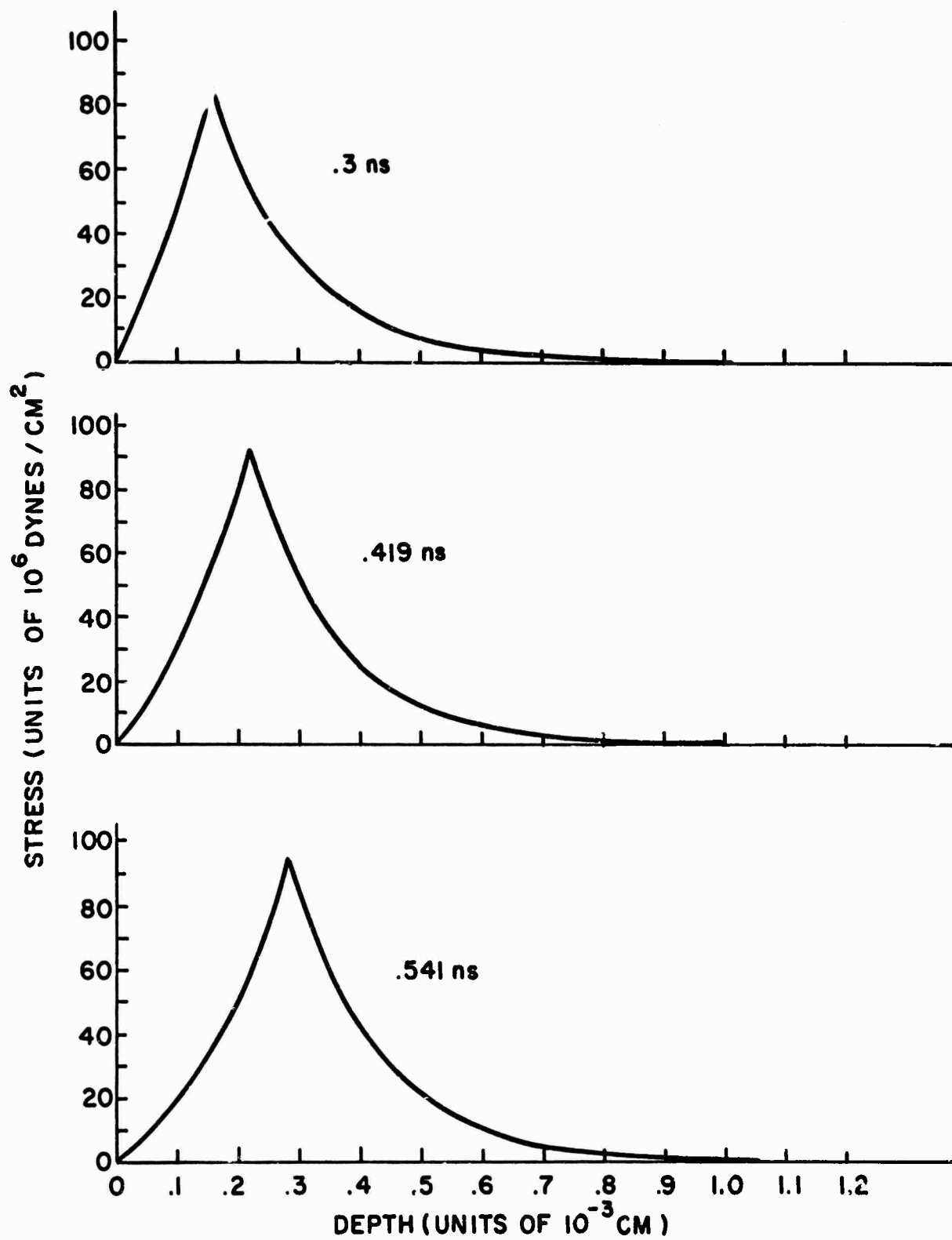


Figure III-9 - Stress Profiles in Carbon Target as Calculated Using PUFF Code for Laser Pulse Depositing 0.3 cal/cm^2

We see, therefore, that we expect a narrow stress pulse propagating into the carbon target. The magnitude of the stress pulse is somewhat smaller for carbon than for the metallic elements which were considered. Qualitatively, for materials of different mechanical properties the behavior of the stress pulses as predicted by the PUFF code is very similar, but the magnitude can differ considerably.

This essentially completes our consideration of the pressure pulses produced in various targets by absorption of laser radiation. We have no plans to verify these computed results experimentally. In order to carry out experimental measurements, the procedure would be to attach pressure transducers to the rear surface of the specimen to be irradiated. However, since the frequencies predicted for the wave in this analysis are much higher than the resonant frequencies of available transducers, we would expect the experimental problems to be difficult and the results to require a considerable amount of interpretation. Therefore, we do not plan to undertake an experimental study of the pressure pulses produced by absorption of the laser radiation.

D. STEADY STATE HEATING

Some preliminary calculations have been made of the temperature that can be achieved by irradiation of different surfaces using a carbon dioxide laser. This type of laser is very desirable in laser-surface interactions as it has a continuous output that can be focused to produce large flux densities (of the order of about 0.1 to 1.0 megawatt/cm²). This type of laser can also be Q-switched repetitively at a high repetition rate and with very constant pulse shape. Thus, if one could expect to achieve heating of the plasma from the surface by Q-switching the laser, very accurate measurements of plasma temperature as well as particle energies and angular distribution could be made using this laser.

In the following calculations it is assumed that we have a thermally thin disc of material with a very large radius that is heated at the center by the focused beam from a carbon dioxide laser. It is assumed, further, that the flux density incident on the disc is constant out to a radius w_0 where w_0 is the gaussian radius of the focused laser beam. This results in a situation in which we effectively have a line source of radius w_0 through the disc and power flows out of this source into the disc. We have assumed that the cooling of the disc takes place by linear convection from both sides. We have neglected radiation because of the difficulties in treating the problem with non-linear heat transfer terms. Also neglected are the phase changes in the material which is considered as an idealized solid with thermal properties independent of temperature. The problem defined above is treated by Schneider ⁽¹⁴⁾. The temperature distribution is given by:

$$T = T_o + \frac{P_o}{2 \pi k \delta \epsilon w_0} \frac{K_0(\epsilon r)}{K_1(\epsilon w_0)}, \quad \epsilon = \sqrt{\frac{2h}{K\delta}} \quad (27)$$

Where:

- K_0, K_1 = Modified Bessel functions of the second kind
- T_o = Ambient temperature in °C
- P_o = Laser power output in watts
- k = Thermal conductivity of material in watts/cm°C
- δ = Thickness of disc
- r = Radial distance from center in cm
- w_0 = Gaussian radius in cm
- h = Unit surface conductance in watts/cm² °K

The equation above has been used to calculate temperature profiles in different materials that might be useful in laser-surface interaction studies, assuming a unit surface conductance of 6×10^{-4} watts/cm² ° K. The materials as well as their thermal conductivities are listed in Table I. The temperature profiles obtained for 20 mil. thick material, assuming a gaussian beam radius of 10^{-2} cm and 10 watts absorbed in the solid are shown in Figure III-10. The temperature profiles shown are those corresponding to steady state conditions, i. e., the temperature profile that will be obtained after irradiation for a long period of time. We have not calculated any transient temperature distributions yet. The most striking feature of Figure III-10 is the fact that the maximum temperature obtained in the material is a very strong function of the thermal conductivity of the material. It is clear from the figure that for a 10 watt power level there are very few materials from which one can expect considerable evaporation as a result of irradiation with a laser. Furthermore, the figure of 10 watts absorbed in the solid is much more restrictive than it would appear at first sight, since metals have extremely high reflectivities at 10.6 microns. Thus in order to obtain 10 watts absorbed into one of these metals a laser power output of from 200 to 500 watts or higher may be required. We can see however that materials of low thermal conductivity such as graphite and plastics, or dielectrics in general, can be raised to very high temperatures with a modest amount of power. In this case 10 watts absorbed in the material means slightly more than 10 watts output from the laser, since absorption coefficients of dielectrics at 10.6 microns are, in general, very large so that the CO₂ laser provides a very efficient heating source for this type of material.

TABLE I

THERMAL CONDUCTIVITY OF SELECTED SOLIDS

<u>Material</u>	<u>Thermal Conductivity (watts/cm°K)</u>
Glass	0.01
Graphite	1.
Platinum	0.7
Pyrolytic Graphite (1)	0.0093
Sodium	1.35
Teflon	0.0025
Titanium	0.2
Tungsten	1.6

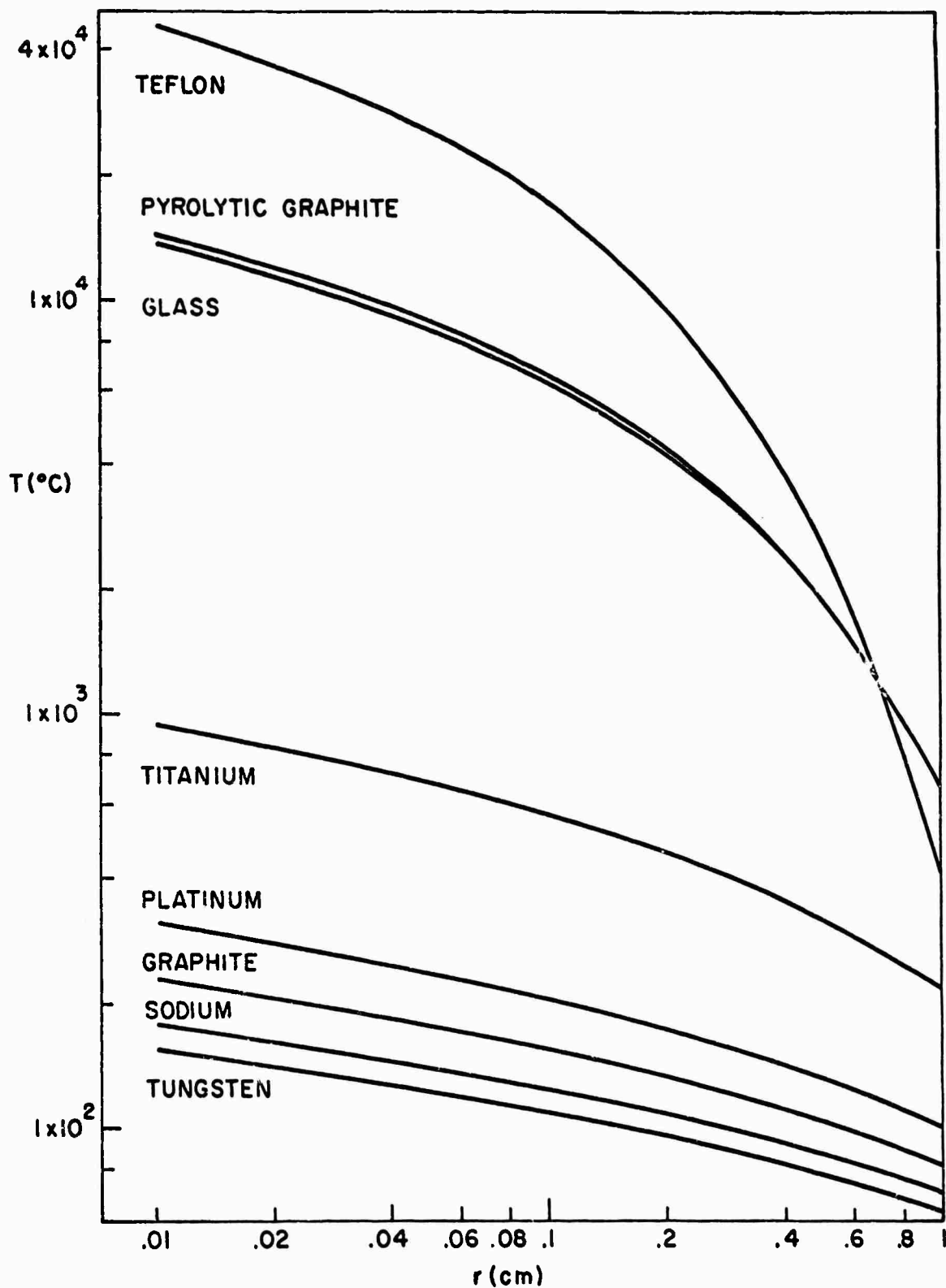


Figure III-10 - Steady State Temperature Profiles Produced in Different Materials Upon Absorption of 10 Watts from a Gaussian Laser Beam Focused to a Radius of 10^{-2} cm. Calculations Assume Power Loss to Ambient by Linear Convection.

SECTION IV

SUMMARY

The work described in this report deals with a number of related topics in the continuing investigation of the interaction of high power laser radiation with absorbing surfaces. This report treats certain selected aspects of this study. This work is to be understood in context with the material presented in earlier reports in this series in which we described measurements on the particle emission produced in a time of flight spectrometer and a quadrupole mass spectrometer (1, 2, 3, 4, 5). When this work is considered together, it helps lead to an understanding of the nature of the processes occurring when the high power laser beam strikes a metallic surface. The topics described here are extensions of measurements or calculations which have been carried out previously as part of this project.

The specific topics treated in this report include measurements on the interaction chamber in which a number of collectors are located around the periphery of a hemisphere with the laser illuminated target at the center of the hemisphere, and a quantitative theoretical evaluation of the particle emission model in laser-surface interactions presented earlier⁽⁵⁾ in which the high energy ions are rapidly heated by absorption of laser light in the inverse Bremsstrahlung process with very little coupling of energy to the neutral molecules in the blowoff material.

The most significant results in this report period are the following:

- (1) Measurements of the angular distribution of the ion emission. The ion emission is maximum in the direction normal to the target surface. In the conditions under which the ions were measured,

they consisted mainly of alkali ions. In the plane perpendicular to the plane containing the laser beam and the target normal, the angular distribution follows approximately a $\cos^2 \theta$ distribution where θ is the angle from the normal to the target. In the plane containing the laser beam and the target normal, preliminary results indicate a more complicated distribution with most of the emission being contained within about 15° of the normal to the target surface.

(2) Measurements of the angular distribution of energies of ions emitted. The energies of ions emitted were determined by the times of flight to the hemisphere. The ion energy is maximum normal to the target surface. In the plane perpendicular to the plane containing the laser beam and the normal to the target the energies are nearly isotropic. In the plane containing the laser beam and the normal to the target surface, the energies fall off to small values at large angles to the normal. The absolute values of the energies, as obtained from retarding potential measurements, indicate agreement with earlier results obtained under similar experimental conditions on the time of flight spectrometer.

(3) Evidence for complicated processes in the interaction chamber which are critically dependent on the voltages applied to the system. To date these results are not well understood.

(4) An indication that the pulse shapes obtained for ion emission in the interaction chamber agree well with the results calculated on a model in which the blowoff material is heated to approximately 20 electron volts near the target surface and then is allowed to expand in an adiabatic free expansion.

(5) Quantitative evaluation of the model in which the heating is produced in absorption of laser radiation by electrons in the blowoff material in the inverse Bremsstrahlung process with relatively little coupling to neutral atoms contained in the blowoff material. This quantitative evaluation indicates that heating occurs at particle densities around 10^{18} cm^{-3} and powers of the order of 10^9 watts/cm^2 . These values are too high for our experimental conditions and it appears as if this model is not adequate to explain the observed phenomena.

(6) Calculation of thermomechanical stress profiles in the target material due to absorption of the laser light. For our experimental conditions the main feature is a sharp short pressure spike propagating into the target. The shape of the pressure pulse is relatively independent of the target material, but the maximum amplitude is dependent on the material. For our experimental conditions the maximum amplitudes do not exceed the yield strength of the target materials.

(7) Evaluation of use of a continuous CO_2 laser in producing laser effects. From temperature profiles calculated on a steady state basis it appears as if the CO_2 laser may be a valuable tool to use in an extension of these measurements, particularly for target materials where the free electron density is low. For such materials the CO_2 laser can provide a very efficient heating source with repetitive pulses. This would allow measurement of the particle emission using synchronous detection methods and possibly eliminate some of the noise problems experienced using a ruby laser with a low duty cycle.

Future plans call for completing and extending the work described in this report. Specifically, we shall complete the investigation

begun on the interaction chamber and carry out retarding potential measurements of the ion energies as a function of angle. We shall carry out the experiment to determine the role of absorption of laser light in heating the blowoff material by illuminating this material with a second higher power laser immediately in front of the target. Optical measurements to identify the ionic species present in the blowoff material through their emission spectrum will be carried out, particularly with a view to determining the time histories of the various species present and to determining if the ionic species are compatible with temperatures in the blowoff material of the order of 20 eV. Finally, we will investigate in more detail the application of a repetitively pulsed CO₂ laser to this type of measurement.

REFERENCES

1. "Mechanisms of Laser-Surface Interactions", by J. F. Ready, E. Bernal G., L. P. Levine, Final Report to Ballistic Research Laboratories on Contract DA-11-022-AMC-1749(A), March 1965. (AD-467, 867)
2. IBID, Final Report on Contract DA-11-022-AMC-1749(A) Mod 2, November 1965. (AD-477, 231)
3. IBID, Final Report on Contract DA-11-022-AMC-1749(A) Mod 2, May 1966. (AD-636, 680)
4. IBID, by J. F. Ready and E. Bernal G., Semi-Annual Report on Contract DA-18-001-AMC-1040 (X), December, 1966. (AD-645, 473)
5. IBID, by J. F. Ready, E. Bernal G., and L. T. Shepherd, Final Report on Contract DA-18-001-AMC-1040(X), May, 1967.
6. E. Archbold and T. P. Hughes, Nature 204, 670 (1964).
7. H. Weichel, P. V. Avizonis, & D. F. Vorderhaar, Phys. Rev. Lett. 19, 10 (1967).
8. B. C. Fawcett et. al., Proc. Phys. Soc. 88, 1051 (1966).
9. C. E. Moore, Atomic Energy Levels, National Bureau of Standards Circular 467, Vol. I, June 15, 1949.

10. S.S. Kuo, Numerical Methods and Computers, Addison-Wesley, (1965), Ch. 7.
11. B.C. Fawcett, D.D. Burgess, & N.J. Peacock, Proc. Phys. Soc. 91, 970 (1967).
12. J.F. Ready, J. Appl. Phys. 36, 462 (1965).
13. L. Spitzer, Jr., "Physics of Fully Ionized Gases," Interscience p. 148.
14. P.J. Schneider, "Conduction Heat Transfer," Addison-Wesley, Cambridge, Mass. (1955).

Unclassified

Security Classification

DOCUMENT CONTROL DATA - R & D

(Security classification of title, body of abstract and indexing annotation must be entered when the overall report is classified)

1. ORIGINATING ACTIVITY (Corporate author) Honeywell Inc. Corporate Research Center Hopkins, Minnesota		2a. REPORT SECURITY CLASSIFICATION Unclassified	
3. REPORT TITLE MECHANISMS OF LASER-SURFACE INTERACTIONS		2b. GROUP	
4. DESCRIPTIVE NOTES (Type of report and inclusive dates) Semi-Annual Report			
5. AUTHOR(S) (First name, middle initial, last name) J. F. Ready, E. Bernal G., and L. T. Shepherd			
6. REPORT DATE November 1967		7a. TOTAL NO. OF PAGES 77	7b. NO. OF REFS 14
8a. CONTRACT OR GRANT NO. DA-18-001-AMC-1040(X)		8b. ORIGINATOR'S REPORT NUMBER(S)	
b. PROJECT NO.		9b. OTHER REPORT NO(S) (Any other numbers that may be assigned this report)	
c.			
d.			
10. DISTRIBUTION STATEMENT This document has been approved for public release and sale; its distribution is unlimited.			
11. SUPPLEMENTARY NOTES		12. SPONSORING MILITARY ACTIVITY U.S. Army Ballistic Research Laboratories Aberdeen Proving Ground, Md. 21005	
13. ABSTRACT <p>This report describes experimental and theoretical investigations of the particle emission produced in a laser-surface interaction. Measurements have been made on the angular distribution of ions emitted from a tungsten target irradiated by a ruby laser at flux densities around 10 to 20 megawatts/cm². In the plane perpendicular to the plane containing the incident laser radiation and normal to the target surface the number of ions emitted follows a $\cos^2\theta$ distribution where θ is the angle from the normal to the target. In the plane containing the laser radiation and the target normal, most ions appear to be emitted within approximately 15° of the normal to the target. The energies of ions are also maximum in the direction normal to the target and fall off as the angle from the normal increases. Calculations on a model for heating an alkali ion plasma by absorption of laser radiation indicate that runaway heating can occur at flux densities around 10⁹ watts/cm² with particle densities around 10¹⁸/cm³. The magnitudes and time histories of shock waves produced in nickel and carbon targets by absorption of laser radiation have also been calculated.</p>			

DD FORM 1473

REPLACES DD FORM 1473, 1 JAN 64, WHICH IS OBSOLETE FOR ARMY USE.

Unclassified

Security Classification

14. KEY WORDS	LINK A		LINK B		LINK C	
	ROLE	WT	ROLE	WT	ROLE	WT
Laser Damage Plasma Mechanisms						